

Aboveground biomass estimates from UAV LiDAR improved via contextual learning in a Norway spruce forest

Jaime C. Revenga¹ | Stefan Oehmcke² | Mana Gharun³
| Flurin Sutter⁴ | Fabian Gieseke² | Katerina Trepekli¹
| Nina Buchmann⁵ | Alexander Damm^{6,7}

¹Institute of Geosciences and Natural Resources Management (IGN), Copenhagen University, Denmark

²Institute of Computer Science (DIKU), Copenhagen University, Denmark

³Institute of Landscape Ecology, Biosphere-Atmosphere Interaction, University of Münster, Germany

⁴Swiss Federal Institute for Forest, Snow and Landscape Research (WSL), Forest Dynamics Research Unit, Switzerland

⁵Department of Environmental Systems Science, ETH Zürich, Switzerland

⁶Department of Geography, University of Zürich, Winterthurerstrasse 190, 8057 Zurich, Switzerland

⁷Eawag, Swiss Federal Institute of Aquatic Science & Technology, Surface Waters – Research and Management, Ueberlandstrasse 133, 8600 Dübendorf, Switzerland

Correspondence

Jaime C. Revenga, Institute of Geosciences and Natural Resources Management (IGN), Copenhagen University, 1350, Copenhagen, Denmark
Email: jar@ign.ku.dk

Forest structure analysis and biomass prediction systems are key tools for advancing forest trait-based ecology and management. Surveys using Unmanned Aerial Vehicles (UAV) and Light Detection and Ranging (LiDAR) systems have contributed to this field with increased accuracy in tree phenotyping. Moreover, methods combining UAV LiDAR surveying and machine learning (ML) have also emerged to enhance estimates of single tree traits. Here, we utilized a UAV LiDAR system to survey a Norway spruce forest in Davos, Switzerland, where a detailed field-based inventory served as ground truth data. Our objectives were (i) to gain insights into variation and gradients of tree height and (ii) to evaluate whether such insights may prove useful as contextual information to improve predictions of stem diameter and tree-level biomass. We segmented the point cloud data scene into individual canopies and treated the LiDAR-derived tree height as the variable of interest. We then used local indicators of spatial association to detect the significant local context, and defined tree neighborhoods within the forest. Then, we extracted metrics from the neighborhoods and introduced them in a ML regression exper-

iment to evaluate predictions of individual tree diameter. The focus was on comparing performance of tree diameter predictions between regression models that either consider neighborhood metrics (i.e. context-aware models), or not. Next, AGB was estimated from the tree height derived from the UAV LiDAR survey, the predicted tree diameter and allometry. The benefits of context awareness were assessed in terms of accuracy gained in estimating AGB. We obtained results of different machine learning methods (i.e. AdaBoost, Lasso and Random Forest) and evaluated these based on nested cross-validation. We applied this approach to two separate tree data sets within the same site, one being clustered and continuous, the other discontinuous and scattered in separate sampling plots. In both cases, we found evidence of enhanced AGB prediction performance in context-aware regressions, where the RMSE was reduced by 4.0% and by 9.1%, respectively. These findings indicate that gradients in tree heights across the ecosystem may proxy for local microclimate, edaphic conditions and biotic factors that influence tree growth, which can be leveraged to enhance predictions of AGB. The method proposed is fully native to UAV LiDAR data.

KEYWORDS

aboveground biomass, , UAV LiDAR, forest structure, functional trait mapping, machine learning, contextual learning, quantitative ecology

1 | INTRODUCTION

Forest aboveground biomass (AGB) is an important component for determining global land carbon (C) budgets. Worldwide, the role of forests is considered essential to understand the exchange of C between the atmosphere and biosphere [1, 2], and a large body of environmental remote sensing (RS) research has advanced our understanding of it. However, current assessments of C-cycling in forest ecosystems present uncertainties, and contrasting findings exist [3], partly caused by the limited accuracy of AGB estimates [4, 5]. This underscores the need for consistent methods to advance quantitative estimates of forest AGB [6].

Traditionally, predictive analyses in forest research and phenotyping from RS data have focused on regressions considering only individual tree attributes as predictors (e.g. tree height, canopy metrics) [7, 8] and fitted allometric models [9], disregarding the influence of neighboring trees on the response variable. Such tree-level analyses

58 have been crucial to improve the characterization of e.g. optical vegetation traits [10], tree dendrometry [11], or
59 species composition [12]. However, these approaches do not account for the influence of the spatial context on
60 the individual tree trait under investigation, be it abiotic factors (e.g. terrain condition, soil depth) or biotic interac-
61 tions (e.g., light interception, nutrient competition). Over time, methods using information of neighboring trees to
62 enhance individual tree trait regressions (i.e. metrics derived from monitoring inventory plots) have been proposed,
63 such as non-linear mixed effects (NLME) methods [13, 14, 15], or competition-based methods [16, 17, 18]. This line
64 of research has shown that considering neighborhood information can improve estimates, and its positive impact has
65 been documented in various tree-level regression analyses, e.g. productivity [19, 20], fuel potential [21] or structural
66 metrics [15, 22, 23].

67 However, despite the utility of current methods that leverage neighborhood metrics such as tree stand infor-
68 mation, from a RS perspective they remain unsatisfactory in some respects. Many of such methods are not directly
69 transferable to a RS framework because they use understory metrics as predictors, which are difficult to survey reli-
70 ably from an above-canopy perspective [16, 17]. Additionally, questions remain about the optimal scale at which such
71 neighborhood metrics become relevant and therefore should be retrieved [19, 20]. However, a common procedure
72 is considering the trees contained in an arbitrarily delineated inventory plot, whose size is defined to fit manage-
73 ment purposes [20]. This approach, although useful for monitoring tasks, can pose the shortcoming of neglecting
74 the spatial scale at which relevant ecological phenomena operate (e.g. the appropriate range at which competition
75 effects are significant), so the analysis remains constrained by the effects of the plot size [13, 14, 15, 16, 17]. To
76 the best of our knowledge, tree-level AGB and trait assessments considering neighborhood information are currently
77 limited due to one or more of the following reasons: (i) they characterize the spatial context with uniquely process-
78 specific indices (e.g. competition pressure from immediate neighbors) [16, 17, 18]; (ii) they calibrate models with
79 neighborhood-metrics retrieved from artificially-bounded inventory plots (e.g. NLME methods) [13, 14, 15]; or (iii)
80 they do not sufficiently account for the spatial scale at which an ecological phenomenon affects the trait under in-
81 vestigation. Moreover, when the relationship between the plot-level predictors used and any ecological phenomenon
82 is described, often ancillary data sources are incorporated (e.g. tree stand age) [17, 24] or poorly quantified forest
83 management metrics, e.g. "stand quality", "site index", "dominance index" [14, 17, 24]. These shortcomings are con-
84 strained by the specific data collection protocol, and currently hinder transferring such methods to an integrated RS
85 framework, which would allow conducting standardized and replicable forest analyses in other regions and at larger
86 scales.

87 From a technical perspective, Unstaffed Aerial Vehicles (UAV) equipped with Light Detection and Ranging (LiDAR)
88 monitoring systems are regarded as particularly versatile [25], accurate and cost-effective tools [26] to contribute to
89 the task of extensive phenotyping, bridging scales in AGB mapping, particularly covering the scale between *in situ*
90 field-based inventories (ca. 0-1 ha) and airborne LiDAR datasets (ca. 0-10⁴ km²) [27, 28]. With a surveying accuracy
91 comparable to field-based measurements, UAV LiDAR monitoring provides datasets (i.e. point cloud data, PCD) that
92 allow individual tree phenotyping at an intermediate spatial scale (1-40 ha). The combination of flexibility and accuracy
93 of UAV LiDAR systems enables quantitative phenotyping of single trees across the landscape (e.g. inspection of tree
94 heights across an environmental gradient), providing extensive and accurate datasets that facilitate analyses at the
95 tree level [7].

96 While both theoretical and technological advances have accelerated the progress of forest AGB research in an
97 unprecedented manner, there is still room for improvement as regards integrating ecological reasoning into AGB re-
98 search. For instance, it is commonly argued that understanding local ecological processes requires monitoring biomass
99 of individual trees [17, 19, 20, 29]. However, the opposite idea is seldom discussed: how and to what extent can com-
100 munity ecology processes be harnessed in tree-level AGB regression experiments? [16, 18] We consider this line of

101 work within AGB research as yet relatively unexplored, with some exceptions. Earlier works have proposed to
102 account for the effects of immediate competition pressure on tree growth with either distance-based [18] or distance-
103 independent metrics [16, 30], and judge such approaches beneficial to improve regression results. For instance, Sun et
104 al. (2019) [16] evaluated the potential of distance-independent and ranking-based tree competition indices to predict
105 tree diameter growth, and found them outperforming competition-unaware prediction models. Similarly, Zhang et al.
106 (2020) [17] ranked trees by competition levels and applied a quantile regression model to enhance predictions of the
107 height-to-diameter ratio.

108 In this scenario, nonparametric ML regression methods seem a sound approach to incorporating a contextual
109 analysis, given their flexibility and that have successfully been integrated into RS forest mapping studies [31]. Such
110 context-based studies [32, 33] have shown in the last decade that the inclusion of information of local context (i.e.
111 information about the surroundings of the target object) may improve model performance [34, 35]. This information
112 can be included in a learning model by either enlarging the receptive field size (i.e. widening the field of view) [31, 35,
113 36] or by incorporating context-aware features that encode neighboring information into the target object [37] (i.e. a
114 specific tree in forestry applications).

115 To our understanding, to date there has not been proposed a standardized UAV LiDAR based approach to add con-
116 text into AGB regression experiments. Furthermore, it has not been fully investigated how spatial patterns and shifts
117 of neighboring tree heights across environmental gradients can reveal the influence of environmental and biotic ef-
118 fects on the individual tree structure. Such patterns, as long as can be surveyed and incorporated into a RS framework,
119 are relevant to AGB research. Specifically, the question that still remains unanswered is how context-awareness can
120 be fully integrated in a RS framework and leveraged to enhance AGB estimates at the individual tree level. Here, we
121 therefore developed a fully integrated UAV LiDAR framework to provide context information into regression analyses,
122 independently from ancillary data sources, or metrics obtained from artificially bounded inventory plots. To meet that
123 end, we i) collected close-range PCD via UAV LiDAR surveying in a coniferous forest, ii) retrieved contextual infor-
124 mation based on the geographic spatial association of tree heights, iii) integrated context into different regression
125 experiments, and iv) evaluated the effect of introducing context-awareness in tree-level AGB estimates, in a Norway
126 spruce forest.

127 This study introduces contextual learning to improve AGB estimates at the individual tree level based on methods
128 fully native to UAV LiDAR data. We posit that incorporating information related to the local forest structure, by
129 informing the regression models of the height distribution of neighboring trees, results in more accurate predictions
130 of tree-level AGB. The findings and method evaluation show that the prediction enhancement caused by including
131 context-awareness, is robust across different models and in two separate datasets within the same mountainous
132 Norway spruce forest. The proposed method is conceived to not rely on additional data sources beyond the UAV
133 LiDAR datasets, in order to ease applicability.

134 2 | MATERIALS AND METHODS

135 2.1 | Study Area

136 The Seehornwald Davos research site (46° 48' 55.2"N, 9° 51' 21.3" E, 1640m a.s.l.) is located in a managed subalpine
137 coniferous forest on the western flank of the Seehorn mountain, near Davos, in the Swiss Alps. The site is labeled
138 as a class-1 forest ecosystem station of the Integrated Carbon Ecosystem Station (ICOS) network [38] where regular
139 forest inventory measurements are collected following standardized protocols. The site is covered by spruce trees
140 (*Picea abies* (L.) Karst., > 99.5 %) with an average height and age of 14m and 100 years, respectively, while some trees

141 reach a height of 40m and an age of 300 years. The stand parameters at the research site include tree density: 639
142 ± 311 tree/ha; basal area: 27.6 ± 16 m²/ha; mean crown area of dominant canopy: 13.2 m²; and mean DBH: 17.7 cm.

143 The site has not been affected by infrastructure development during the 20th-21st centuries. Since 1930, grazing
144 livestock in the forest was abandoned, and the site is sustainably managed according to the Swiss Forest Law (1876,
145 revised until 2017) [39]. Maps dating back to 1845 reveal minimal changes within the Davos-Seehornwald forest
146 site, while slight effects of local harvests are noticeable, particularly on steeper slopes of the eastern flank, and forest
147 regrowth at the timberline can also be observed [40]. Patchy vegetation (i.e. dwarf shrubs and mosses) covers around
148 30% of the forest floor (acidic ferralic podzols), which lies on a mixed silicious and dolomitic bedrock. The research
149 site is part of national (LWF [41], TreeNet [42], SwissFluxNet [43]) and international research networks (ICOS [44],
150 ICP Forests [45], eLTER [46]).

151 The considered study area spans over 33 ha (Figure 1, b), and the terrain conditions are representative of the Alps
152 around the Landwasser valley, i.e. a varying steepness of $23 \pm 14^\circ$. The site lies on the eastern flank of the valley, so
153 most of the slopes face west-southwest, i.e. mean slope aspect is 230° .

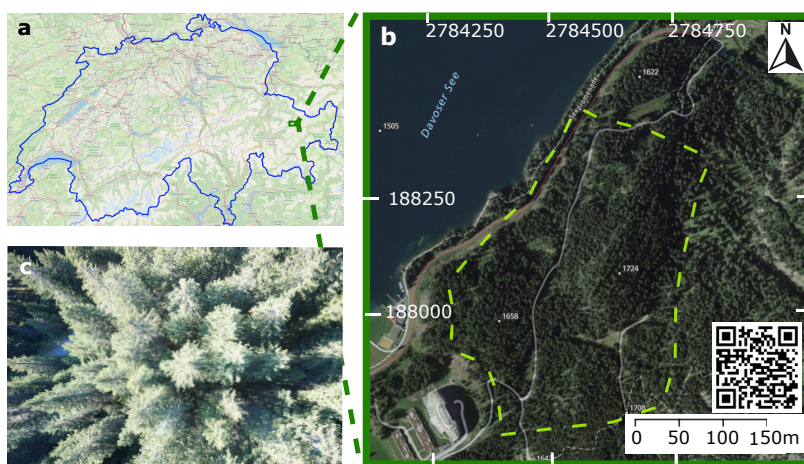


FIGURE 1 a: Location of the study site; the blue outline delineates the national territory of Switzerland (adapted from open.sourcemap.com). b: Orthoimage of the study site (adapted from swisstopo.admin.ch); coordinate units are in m, with LV95 as a projected reference system; the QR code links to additional information of the study site. The dashed yellow line shows the boundaries of the research site c: RGB image of forest canopy from a nadir angle taken during the survey.

154 2.2 | UAV LiDAR Survey and Field-Based Measurements

155 We used a UAV-borne LiDAR system mounted to a DJI Matrice 600 Pro payload at a 90° pitch angle, and same heading
156 and roll as the UAV platform. The system included a discrete infrared LiDAR scanner (M8 sensor, Quanenergy Systems,
157 Inc. Sunyvale, CA, USA) and the corresponding state-of-the-art inertial and navigation systems. In addition, we used
158 a ground based Global Navigation Satellite System (GNSS, Trimble R8) during the UAV LiDAR survey, set up in post-
159 positioning kinematic (PPK) mode, which logged real-time satellite coverage (cf. Revenga et al. 2022 [47] for details on
160 the airborne and ground system). The coupling of the satellite coverage data with the UAV-based laser and navigation
161 data produced, allowed the generation of georeferenced point clouds, following Davidson et al. (2019) [48].

162 Data were acquired with a UAV flight height adapted to the terrain and tree height (Figure 2, a), ensuring a >20%
 163 overlap between individual LiDAR scans of ca. 50m width and 250 points/m². The surveys were conducted in October
 164 2021, coinciding with the end of the forest growing season. Figure 2 (a) shows the trajectories of the individual UAV
 165 LiDAR flights during the survey campaign. While the standard survey coverage followed a regular auto-pilot flight
 166 grid, certain flight lines had to be manually piloted to adapt to the topography and local forest structure. The digital
 167 elevation model of the study area is provided in Supporting Information (Annex V), to help to understand differences
 168 in flight heights.

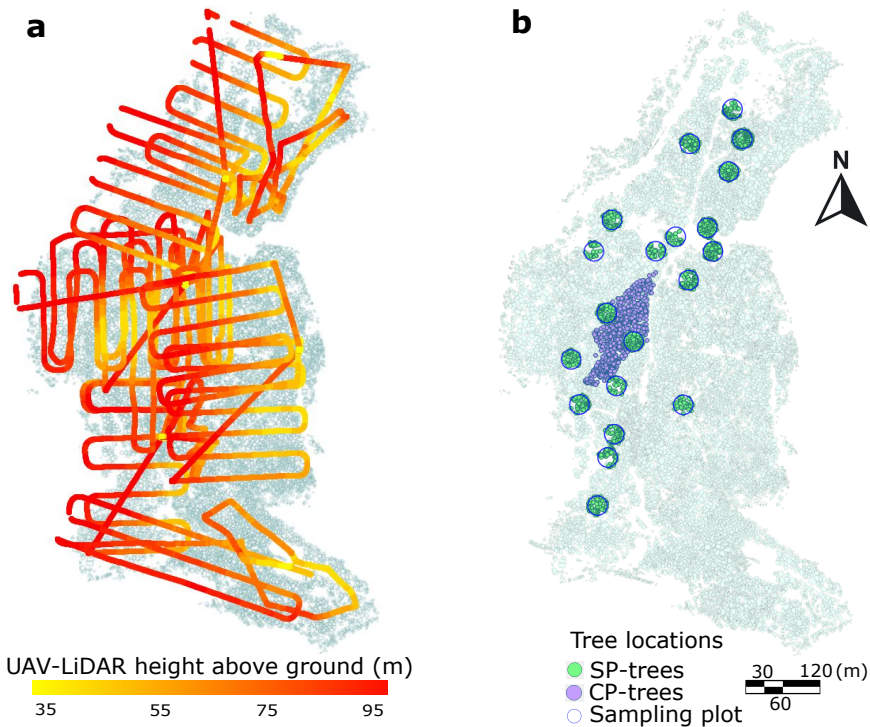


FIGURE 2 a: Trajectories of individual flights during survey of the Unstaffed Aerial Vehicle (UAV) Light Detection and Ranging (LiDAR) sensor; color gradient indicates height above ground during survey. b: Spatial distribution of field-based forest inventory. Dots represent the locations of the ground truth labels. The sampling plot-trees (SP-trees, N = 1635 trees) are shown in green; the control plot-trees (CP-trees, N = 845 trees) are shown in purple. In both a and b, the underlying polygon dataset shows the individual tree canopies (ITC) after the canopy height model (CHM) segmentation.

169 The field-based measurements (shown in Figure 2, b) are taken on a yearly basis as part of a long-term ecosystem
 170 monitoring initiative—jointly organized by ICOS [44] and the Swiss Federal Institute for Forest, Snow and Landscape
 171 Research (WSL) [41]. Based on standardized methods (i.e. *Sanasilva Inventory* protocol) [49], expert field workers
 172 monitor tree crown status, focusing on three groups of indicators: variations in size, density and color. The number of
 173 trees that have died since the previous survey, as well as the new ones that reached a minimum DBH of 5 cm are also
 174 recorded [50]. Tree height and DBH are monitored with a high-precision digital rangefinder (i.e. Vertex Laser Geo)
 175 and a standard calliper, respectively.

176 We treated two different datasets separately as ground truth measurements within the same study area: control
177 plot trees (CP-trees, 4 adjacent monitoring units) and sampling plot trees (SP-trees, 20 scattered units of 15m radius).
178 The two datasets (i.e. SP- and CP-trees) are monitored by different research groups on the field and protocols pre-
179 sented minor differences between both datasets. Two main factors led us to consider both datasets separately: (i)
180 the CP-dataset is clustered and spatially continuous, while the SP-dataset is spatially discontinuous and distributed
181 along the study site (Figure 2, b); and (ii) the two datasets present differences in morphological trait distribution (see
182 Supporting Information, Annex IV). Figure 2 (b) shows the spatial distribution of the field-based forest inventory. The
183 CP tree position was recorded using a Leica GPS1200 total station. The location and size of the sampling plots were
184 defined according to ICOS protocols [51]. The center location of the SP plots was determined using a GNSS Leica
185 CS20 (antenna GS15) with a real-time kinematic (RTK) signal (accuracy measurements ranges from 0.03m to 0.7m).
186 Next, the trees in the SP plots were positioned by measuring the azimuth with a field goniometer, while the horizontal
187 distance and the inclination from the plot centers was determined using a Vertex Laser Geo meter. The accuracy of
188 foot location of trees in the SP plots is within 0.5m and 1.2 m. The field-based inventories used as ground truth con-
189 tain measurements taken between October 2019 and July 2021. The changes in structural traits of max. two years
190 between field-based measurements and UAV LiDAR data acquisition were considered negligible for the purposes of
191 this study (i.e. no disturbance events occurred).

192 2.3 | Method setup

193 The workflow followed in this study is presented in Figure 3. Initially, the PCD generation followed the approach de-
194 scribed in Revinga et al. (2022) [47]. The resulting PCD scene was normalized and rasterized to obtain a canopy height
195 model (CHM), which in turn was subject to individual tree crown segmentation [52] producing a two-dimensional poly-
196 gon dataset. For the CHM segmentation, we utilized a watershed algorithm that is specifically designed for coniferous
197 forests [52] (implemented in the LiDAR360 software [53]). The match between field-based measurements and indi-
198 vidual tree crown (ITC) polygons was conducted based on the closest distance between the field-based GNSS point
199 measurement and the ITC polygon centroid.

200 In order to ensure that only the LiDAR-detected trees would be accounted for in the regression experiment,
201 a pre-processing task was undertaken (marked * in Figure 3). First, understory trees that passed unnoticed to the
202 UAV LiDAR survey were removed. Second, we filtered clumped trees based on tree height by selecting the field-
203 based measurement of the highest tree when two ground measurements were less than 1 m apart, while removing
204 the measurement of the shorter tree. Third, we corrected for a crown shift effect, i.e. some high and skewed trees
205 were affected by the presence of a smaller neighboring tree (affecting less than 5% of the trees) being closer to its
206 corresponding ITC polygon centroid, thus introducing a wrongly allocated label between the field-based measurement
207 and the LiDAR-derived metrics.

208 Afterwards, using the LiDAR-derived height as polygon attribute, we calculated the distance at which the spatial
209 autocorrelation of tree height was most significant in order to define the optimal neighborhood size (as explained
210 in Section 3.1). Once the optimal neighborhood size had been defined, we conducted the local indicators of spatial
211 association (LISA) analysis [54, 55] and outlier analysis [56, 57] to retrieve neighborhood metrics. Finally, two separate
212 supervised regression experiments were performed, in order to predict DBH based on LiDAR-derived metrics: one
213 including the neighborhood metrics (context-aware regression), the other without taking those metrics into account
214 (context-unaware regression). Finally, AGB was estimated from the predicted DBH via an allometric function (as
215 defined in Eq. 5).

216 In parallel, we conducted a second task to characterize the morphometry of tree assemblages (i.e. groups of

217 adjacent trees fulfilling a specific criterion of height similarity, as explained in Section 2.3) stemming from the ITC
 218 polygon dataset. Prior to the morphometric analysis of tree assemblages, a second pre-processing task was conducted
 219 (marked ** in Figure 3). First, ITC polygons were merged based on either local Moran's I_i [54] or SL_i [58] (see Section
 220 2.3). These new larger polygons describe the two-dimensional projection of tree assemblages. Then, as our interest
 221 focused on the extent and shape of the tree assemblages, the inner borders of the merged polygons were disregarded.
 222 To reduce computation time, the polygon shapes were simplified by reducing the number of vertices and edges to 70 %
 223 while keeping the polygon shape.

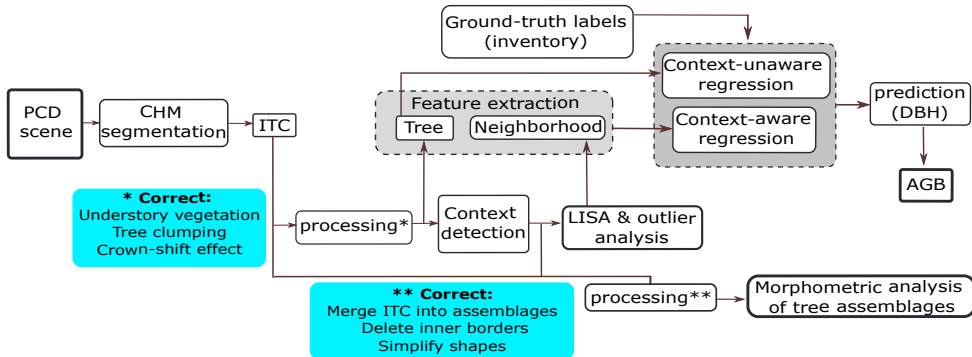


FIGURE 3 Workflow followed in this study. PCD: point cloud data, CHM: canopy height model, ITC: individual tree crown, LISA: local indicators of spatial association, DBH: diameter at breast-height, AGB: aboveground biomass. The two colored boxes describe the subtasks constituting each of the processing steps, marked * and ** in the diagram.

224 | Definition of Context Via Tree Heights in the Neighborhood

225 We determined the distance at which neighborhood metrics should be calculated (i.e. how many surrounding trees
 226 should be accounted as neighbors) based on local similarity of tree height. Accordingly, the selection of an appropriate
 227 neighborhood size around each individual tree (i.e. context detection) [59] was calculated through the analysis of
 228 spatial autocorrelation of tree height as function of incremental distance, as in previous studies [60]. Based on the
 229 global peak in the significance of spatial autocorrelation, we defined a characteristic distance within which all included
 230 trees should be considered as neighbors. Then, all so-defined neighbor trees were accounted for to compute context-
 231 aware metrics.

232 The local context information was encoded as metrics derived from the distance-weighted individual tree heights
 233 in each neighborhood, calculated at each tree location. Specifically, the metrics computed to define the local context
 234 were: local Moran's I [54] (i.e. an estimate of local significance of tree height similarity with respect to the global
 235 variance); and (SL_i) of tree height (i.e. a weighted average of heights calculated entirely locally) [58].

236 Local Moran's I_i is a well-established distance statistic in spatial data analysis [61], used for detecting local spatial
 237 autocorrelation and included within the family of LISA methods [54, 55, 58]. Similarly to other geostatistics meth-
 238 ods [62], it relates attribute similarity with locational similarity, mapping autocorrelation across the geographic space.
 239 In the following definitions, σ is the global sample standard deviation of tree height; n and m represent the total num-
 240 ber of instances (i.e. all trees in the forest) and the number of neighbors to each tree, respectively; y_i indicates the
 241 magnitude of interest at a particular point of interest (i.e. tree height) while the overline (i.e. \bar{y}) indicates the global

242 average; $w_{i,j}$ indicates the distance weighting of each neighboring tree (here defined as inverse distance weighting);
 243 subindexes i and j indicate the tree of interest and a neighbor tree, respectively. Let y_1, \dots, y_n be the tree height
 244 values of all the n trees in the dataset. Then, the Local Moran's I_i [54] is defined as

$$I_i = \frac{y_i - \bar{y}}{\sigma^2} \sum_{j \in \mathcal{N}_i, j \neq i} w_{i,j} (y_j - \bar{y}), \quad (1)$$

245 where $\mathcal{N}_i \subset \{1, \dots, n\}$ is the set of indices corresponding to the nearest neighbors of tree $i \in \{1, \dots, n\}$ in the
 246 overall set, where

$$\bar{y} = \frac{1}{n} \sum_{i=1}^n y_i, \quad (2)$$

247 and

$$\sigma = \sqrt{\frac{\sum_{i=1}^n (y_i - \bar{y})^2}{n - 1}}, \quad (3)$$

248 are the global average height and the global sample standard deviation, respectively. It should be noted that
 249 insofar I_i includes global metrics (such as n , σ and \bar{y}), it is not entirely locally computed, but may present correlation
 250 with global features (i.e. characteristics derived from the entire dataset; cf. Westerholt et al. 2018) [63].

251 The Spatial Lag (SL_i) of tree height for a tree i is a spatial smoother [64] defined as:

$$SL_i = \sum_{j \in \mathcal{N}_i, j \neq i} w_{i,j} y_j \quad (4)$$

252 where the elements of the spatial weights matrix ($w_{i,j}$) are row-standardized, so that $\sum_{j \in \mathcal{N}_i, j \neq i} w_{i,j} = 1$. Therefore,
 253 SL_i can be seen as a weighted average of the heights of neighboring trees [65].

254 The neighborhood metrics finally chosen as context-aware predictors are the following: local Moran's Index (I_i),
 255 z-score of I_i , p-value of I_i , z-transformed value of I_i and SL_i —computed at 20 m, 30m, 40m and 50m distance bands.
 256 Additionally, the mean heights of the k-nearest trees, with $k \in (5 - 75)$, were also included as predictors. Likewise,
 257 we also included the topographic wetness index (TWI) [66] in order to evaluate the relative predictive performance of
 258 neighborhood metrics with respect to a well-established environmental variable as tree-growth predictor [67]. TWI
 259 is a steady state wetness index used to evaluate topography-dependent surface hydrology processes. According to
 260 the established definition [66], TWI is calculated as $\frac{a}{\tan(b)}$, where a represents the upslope area draining through
 261 the point of interest, and b indicates the local slope. The parameterization considered to calculate TWI followed the
 262 suggestions of Kopecký et al. (2021) [68] for soil moisture estimation. In order to discern how much the contribution
 263 of TWI is influenced by granularity, we calculated it at a 2 m^2 resolution, and resampled to 5 and 10 m^2 , via bilinear
 264 interpolation. Therefore, TWI was included at a spatial resolution of 2, 5 and 10 m^2 as separate predictors.

265 Finally, we included in the regression experiments predictive features informing of local neighbor dissimilarity,
 266 i.e. local outliers of tree height. We detected local outliers using Local Outlier Factor [56] and Isolation Forest [57]

267 algorithms. The evaluation of these features allowed us to discern between the contribution of local similarity features
268 (i.e. Local Moran's I_i and SL_i) and that of the local outliers.

269 | Tree Assemblages' Morphometry

270 Utilizing the neighborhood metrics defined above, we computed tree assemblages within the study site. This enabled
271 us to investigate whether the morphometry of such forest sectors would be useful as predictors of individual tree
272 attributes (i.e. DBH, AGB). In order to define the tree assemblages, both local Moran's I_i and SL_i were computed at
273 the optimal distance band to obtain neighborhood metrics, i.e. based on the global peak in the significance of spatial
274 autocorrelation of tree height as a function of distance (using ArcGIS Pro) [69].

275 Tree assemblages were therefore defined as geographically continuous groups of trees delineated according to
276 either (i) variation of local Moran's I_i of tree height, or (ii) according to quantiles of SL_i of tree height. The rationale
277 for using two different statistics to calculate tree neighborhood metrics and thus delineate different tree assemblages
278 was that while SL_i is entirely locally calculated, local Moran's I_i includes global features (and is therefore sensitive to
279 the statistical characteristics of the dataset as a whole), as explained in Section 2.3. In order to discern which of the
280 two approaches resulted most convenient in delineating tree assemblages (the former *entirely* local; the latter only
281 *partially* local), both were included.

282 Tree assemblages defined according to local Moran's I_i are geographically continuous groups of trees with signif-
283 icantly different heights than the global tree height average, and they also lie in a region with significantly different
284 neighbors. Local Moran's I_i identifies regions where the clustering of either high or short trees occurs. In the standard
285 notation [58] (i.e. *High-High* or *Low-Low*), the first term refers to the individual tree and the second to the neighborhood
286 (e.g. a tree belonging to a *High-High* assemblage is a "significantly high tree" in a "significantly high neighborhood").
287 The areas not showing statistical significance (that we thresholded at p-value ≥ 0.002) were labeled as *Not-Significant*.
288 The significance test is based on random permutations ($n = 499$) of neighboring tree-height values at each step in the
289 computation. The number of permutations and p-value indicate that, under the null hypothesis (i.e. tree heights being
290 randomly distributed), a single tree canopy is likely to be wrongly classified with a probability of 0.002, which was
291 deemed sufficient for the purpose of evaluating tree assemblage morphometry (i.e. if 1 out of 499 trees is wrongly
292 attributed to a neighborhood, the morphometry of the assemblage will not change markedly). Then, for every permu-
293 tation, a local Moran's I_i value was calculated by randomly rearranging the tree heights of neighboring values. The
294 result is a randomly generated reference distribution of expected local Moran's I_i that is compared against the ob-
295 served local Moran's I_i (Eq. 1) [55]. In this way, tree assemblages defined according to local Moran's I_i are classified
296 as: *High-High*, *Low-Low*, or *Not-Significant*.

297 Likewise, tree assemblages defined according to SL_i of tree height are geographically continuous groups of trees
298 delimited according to the local weighted average of tree height [65], as defined above (Eq. 4). For the purpose of
299 this study, 5 subdivisions based on quantiles were deemed convenient, rendering a classification of tree assemblages
300 based on SL_i ranking as: *Highest*, *High*, *Mid*, *Low* and *Lowest*.

301 The morphometric analysis examined the outer boundaries of the tree assemblages, defined either by local
302 Moran's I_i or SL_i of tree height, as defined above. Twenty basic morphometric parameters as well as 20 derived
303 parameters were calculated for each type of tree assemblage. The 20 basic morphometric variables are simple param-
304 eters obtained by fitting elemental geometric shapes to each tree assemblage polygon (e.g. area of maximum inscribed
305 circle), and basic positional parameters (e.g. XPOL, which is the X coordinate of the centroid of the tree assemblage
306 polygon). The 20 derived parameters are adimensional metrics (except for concavity [70], measured in m) computed
307 from the 20 basic morphometric variables, as explained in Güler et al. 2021, [71] (details are given in Supporting Infor-

308 mation, Annex I). The morphometric analysis of tree assemblages was conducted using PolyMorph-2D algorithm [71],
 309 which is a toolbox for the morphometric analysis of vector-based polygon objects, available as a plug-in for the open
 310 source JumpGIS software [72].

311 | Regression Models Selected

312 The regression experiments were designed to predict DBH, since AGB is a variable determined by the combination
 313 of DBH, height and wood density [9]. Instead, DBH is directly measured in the field, which makes it a better defined
 314 regression target. Therefore, the model estimates of AGB were derived from the DBH prediction outputs by means of
 315 an allometric fit (Eq. 5). Predicting DBH, instead of AGB directly was chosen as more suitable, as it avoids burdening
 316 the learning models with the statistical error contained in the allometric fit. Three feature-based regression methods
 317 were selected: namely AdaBoost [73, 74, 75], Lasso [76] and Random Forest [77] regressors. The AdaBoost regressor
 318 employs a gradient-boosting method that relies on stage-wise additive expansions. Its effectiveness stems from com-
 319 bining weak learners, i.e. decision trees, to form a generalized prediction hypothesis. Lasso, on the other hand, is a
 320 linear model with an $L1$ prior penalty acting as a regularizer [78]. Random Forest is a well known tree-based ensemble
 321 regression method. In our case, all three regression methods utilize the features derived from the ITC polygon dataset
 322 resulting from the CHM segmentation.

323 Context-unaware regressions were defined as those in which a learning model performs DBH regression by taking
 324 as predictors only individual tree attributes derived from the ITC polygon dataset (i.e. tree height, canopy area and
 325 canopy perimeter), as it is a common approach [8]. On the other hand, we defined context-aware regressions as those
 326 regressions in which context-aware features are additionally introduced as input in the predicting feature space. These
 327 were either neighborhood metrics, e.g. SL_i of tree height, or TWI at different spatial resolutions (see Section 2.3).
 328 For every model predicting DBH from individual tree attributes (i.e. context-unaware conditions) we implemented a
 329 context-aware counterpart. This allowed us to evaluate the impact of context on regression model performance.

330 | Model Training and Validation of Results

331 A hard validation of AGB is not possible without harvesting trees destructively, which raises obvious ethical, legal and
 332 economic issues. Instead, non-invasive methods that use RS data and allometric functions are the standard procedure
 333 for estimating AGB [79]. Here, we estimated AGB from tree height, DBH, wood density and an allometric function
 334 (eq. 5). The regression analyses conducted are focused on comparing performance of predictions on DBH between
 335 models (i) "context-unaware" and their (ii) "context-aware" counterparts.

336 We chose DBH as the variable to test model predictions, which is a tree morphological trait contained in the field-
 337 based forest inventory, and therefore directly measured by *in situ* monitoring. Next, in order to assess the benefits of
 338 including context in the regression models, we compared results using AGB of individual trees. Hence, AGB estimates
 339 were derived via species-specific allometric and wood density functions, tree height retrieved via UAV LiDAR, and
 340 DBH predicted via ML regression. Specifically, the allometric model used was the one proposed by Dalponte and
 341 Coomes (2016) [9]:

$$AGB_{tree} = \alpha \cdot WD_{spruce}^{\beta} \cdot (DBH - d_0)^{\gamma} \cdot H^{\delta}, \quad (5)$$

342 where the wood density value (WD_{spruce}) was taken from Alpine spruce dendrometric models [80], DBH was

343 predicted via ML regression and height (H) was extracted from the UAV LiDAR data. $\alpha, \beta, \gamma, \delta$ and d_0 are species-
344 specific fitted allometric parameters [81], obtained from allometric fits to harvested spruce trees by the Forestry and
345 Wildlife Service Agency of the province of Trento (an Italian neighbouring province southeast from the study site, also
346 used in Dalponte and Coomes, 2016) [9], and we consider them applicable to the Seehornwald Davos research site.
347 At all events, for the purpose of assessing the benefits of a context-aware approach, the specific characteristics of
348 the allometric fit used are negligible, as it is only used to quantify a difference in terms of AGB, and both types of
349 predictions (unaware and aware) take the same equation. Therefore, the predicted value of DBH (in either aware or
350 unaware conditions) was input into Eq. 5, in order to obtain model predictions of AGB. This allowed to compare AGB
351 predictions with the ground truth values of AGB, which were similarly obtained via the field-based measurements
352 (provided by the regular tree-monitoring campaigns of ICOS [44] and WSL [41]) and Eq. 5.

353 For training and validating the regression models, the instances with empty ground truth labels were initially
354 removed (i.e. trees with no DBH or tree height recorded). Afterwards, data stratification was performed via five
355 commonly used percentiles (i.e. 0-10, 10-25, 25-50, 50-75, 75-90, 90-100) to ensure that the input data are inde-
356 pendently drawn from an identical sample distribution (IID assumption) [82]. This assured us that most parts of the
357 target distribution are represented, in particular the tail ends.

358 The technique used to estimate model prediction error consisted of a nested cross-validation (NCV) scheme [83].
359 Following the NCV scheme, we divided the input dataset into 10 inner and 10 outer folds. In NCV, the results in the
360 inner folds report of the training performance, and they are used for model optimization, while the mean performance
361 on the outer folds is the one used for model evaluation. The model inspection technique used to evaluate predictors'
362 influence on the DBH regression results was the permutation importance method as proposed by Altmann et al.
363 (2010) [84]. The feature-elimination procedure consisted of eliminating progressively those predictors that presented
364 a negative mean importance, as they were considered harmful to the model's performance. The significance of the
365 enhancement in context-aware predictions and effect size was assessed using Wilcoxon signed-rank test [85] and
366 Cliff's Delta analysis [86], respectively.

367 3 | RESULTS

368 3.1 | Context Detection and Tree Assemblage

369 The analysis of spatial autocorrelation of tree height as function of incremental distance resulted in a maximum sig-
370 nificance at a distance of 40 m. Figure 4 (a) shows the calculation of local Moran's index (I_i) of tree height at different
371 distance bands. Figure 4 (b) shows the z-score of I_i obtained at each distance band, resulting from comparing the
372 observed I_i and the expected I_i under the tree height randomness assumption (details included in the Annex II). As
373 a precaution, we ran context-aware regression experiments including also context features retrieved at shorter (i.e.
374 20m, 30m) and larger (i.e. 50m) distances than the optimal range (i.e. 40m). The context features retrieved at these
375 distances and that contributed to improved predictions of DBH (i.e. 20, 30, 40 50m) were all included in the final
376 regression models.

377 In Figure 5, panels a and b show the spatial distribution of tree assemblages calculated using either local Moran's
378 I_i or SL_i of tree height, respectively, at 40m range. While both types of assemblages show similarities as regards
379 extent, morphometry and location, SL_i captures more local variability. This is not only due to a higher discretization
380 (5 groups in SL_i , vs. 3 groups in local Moran's I_i), but also to the fact that SL_i is insensitive to the variance in the
381 dataset beyond the range of its neighborhood, as explained in Section 2.3.

382 The morphometric analysis provided 40 additional features that were evaluated as potential predictors of DBH.

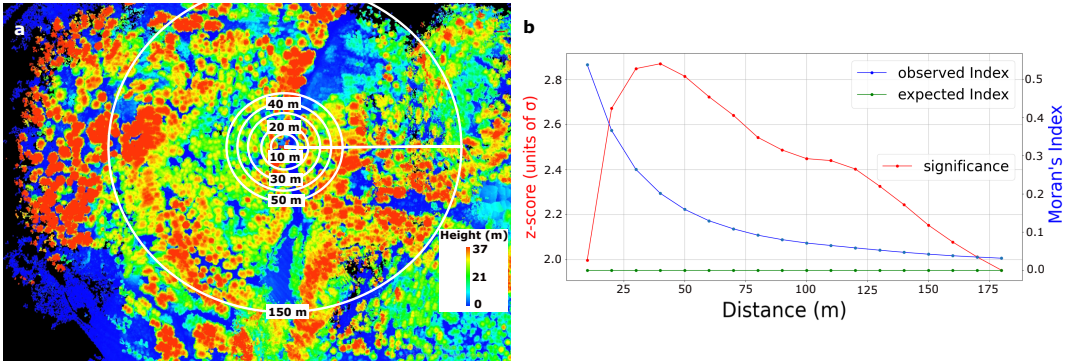


FIGURE 4 Context detection. **a:** Normalized point cloud data (PCD) scene colored by tree height overlaid with a selection of the appropriate radii for defining the neighboring context. **b:** Autocorrelation of tree height as function of distance. The red line shows the number of standard deviations (σ) that an observation is away from the expected value (under the assumption of heights being randomly distributed). The blue and green lines show the actually observed local Moran's Index and the expected value under randomness assumption, respectively.

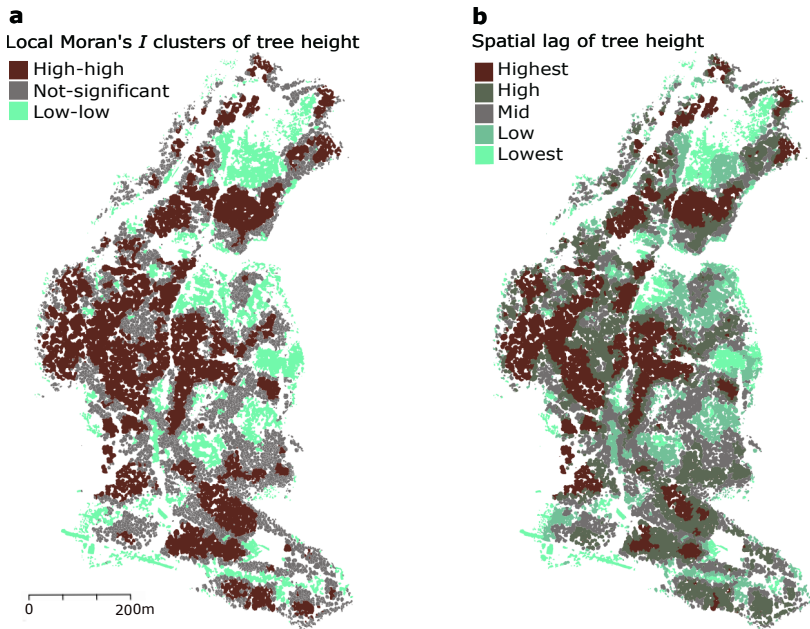


FIGURE 5 Tree assemblages defined by local similarity of tree height. **a:** Delineated according to local Moran's I_i of tree height. **b:** Delineated according to spatial lag of tree height.

383 In Figure 6, panels a and b visualize the results of the morphometry analysis of tree assemblages defined by local
 384 Moran's I_i and by SL_i , respectively. The circular barplots show the average magnitude as bar lengths, and the standard
 385 deviation as dots. Both mean and standard deviation values are shown as min-max scaled (across assemblage types)

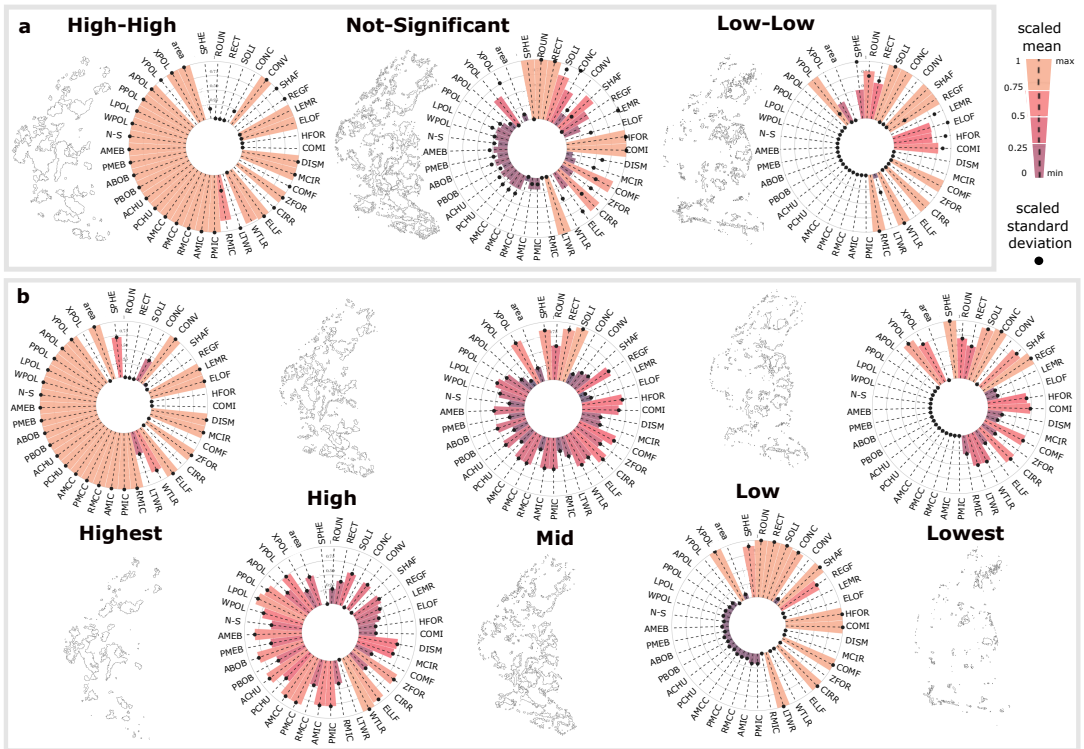


FIGURE 6 Morphometric analysis of tree assemblages grouped by (a) local Moran's I_i , and (b) by spatial lag of tree height. Bar length and color gradient represent the mean value, while black dots represent the standard deviation (SD) over all tree assemblages. Both mean and SD are scaled (min-max) to allow comparison of all metrics across assemblage types on the same axis—i.e. for every morphometric variable, the highest value of a certain assemblage type is replaced by 1, the minimum value is replaced by 0, and the intermediate values are linearly interpolated in between the range (0-1). YPOL: northing of centroid of the tree assemblage; XPOL: easting of centroid of the assemblage; APOL: area of polygon (P); N-S: defined as $|\sin(\text{azimuth})|$, shows the alignment of the main axis of P with the North-South direction; PPOL: perimeter of P; LPOL: major axis length (L) of P; WPOL: minor axis length (W) of P; ABOB: area of the bounding box fully containing P; PBOB: perimeter the bounding box fully containing P; AMEB: area of the minimum enclosing box fully containing P; PMEB: perimeter of the minimum enclosing box fully containing P; ACHU: area of containing hull; PCHU: perimeter of convex hull fully containing P; AMCC: area of the minimum circumscribed circle (MCC); PMCC: perimeter of MCC; RMCC: radius of MCC; AMIC: area of maximum inscribed circle (MIC); PMIC: perimeter of MIC; perimeter of MCC; RMIC: radius of MCC; LTWR: length-to-width ratio [87]; WTLR: width-to-length ratio [88]; ELLF: ellipticity factor [89]; CIRR: circularity ratio [90]; ZFOR: Zavoianu's form factor [91]; COMF: compactness factor [71]; MCIR: Miller's circularity ratio [92]; DISM: dispersion measure [90]; COMI: complexity index [71]; HFOR: Horton's form factor [87]; ELOF: elongation ratio [93]; LEMR: lemniscate ratio [94]; REGF: regularity factor [89]; SHAF: shape factor [89]; CONV: convexity [95]; CONC: concavity [70]; SOLI: solidity [96]; RECT: rectangularity [97]; ROUN: roundness [95]; SPHE: sphericity [98].

386 to present all variables on the same radial axis and to ease visual comparison, i.e. for every morphometric variable,
 387 the highest value is replaced by 1, the minimum is replaced by 0, and the intermediate values are linearly interpolated
 388 between 0-1.

389 It can be observed (Figure 6) that the morphometric variables follow very similar trends when tree assemblages

are defined based on local Moran's I_i or SL_i . However, an observed difference between SL_i and local Moran's I_i was found in the heteroscedasticity of the morphometric variables calculated. In the former case, we observed that the variance of all metrics scaled with magnitude (i.e. constantly increasing variance), while in the latter an irregular trend was found (i.e. an uneven trend in the variance). We visualized these observations in the distribution of scaled mean values and scaled standard deviations in Figure 6, a and b.

While not for all variables a systematic trend was found, for several basic morphometric variables a linear positive correlation between them and SL_i was observed, as shown by the calculated Pearson coefficient (ρ). This is the case for polygon area ($\rho=0.95$), perimeter of polygon (PPOL; $\rho=0.98$) and radius of the minimum circumscribed circle (RMCC; $\rho=0.98$). Additionally, a positive correlation was found for some derived morphometric variables, namely: length-to-width ratio (LTWR; $\rho=0.75$) [87], circularity ratio (CIRR; $\rho=0.88$) [90], compactness factor (COMF; $\rho=0.89$) [71], dispersion measure (DISM; $\rho=0.90$) [90], complexity index (COMI; $\rho=0.88$) [71], lemniscate ratio (LEMR; $\rho=0.81$) [94], regularity factor (REGF; $\rho=0.82$) [89], and concavity (CONC; $\rho=0.96$) [70]. Conversely, other morphometric variables showed a decreasing trend with increasing SL_i . A clearly negative correlation between SL_i and the following derived morphometric variables was found: Miller's circularity ratio (MCIR; $\rho=-0.88$) [92], Horton's form factor (HFOR; $\rho=-0.88$) [87], elongation factor (ELOF; $\rho=-0.83$) [93], shape factor (SHAF; $\rho=-0.95$) [89], rectangularity (RECT; $\rho=-0.85$) [97] and roundness (ROUN; $\rho=-0.69$) [95].

3.2 | AGB Predictions: Aware vs. Unaware of Local Context

Regression experiments including context-aware features improved predictions of DBH consistently (see Tables 1 and 2), resulting in spatially resolved enhanced tree-level AGB predictions via allometry (Eq. 5). Although consistent, the degree of prediction enhancement differed between both datasets considered. Predictions in the CP-dataset observed a lower enhancement in comparison to predictions in the SP-dataset. For instance, RMSE was reduced by 9.1% (SP-dataset) vs. 4.0% (CP-dataset), and R^2 increased by 3.5% (SP-dataset) vs. 3.2% (CP-dataset). This was expected, due to less variability in context in the CP-dataset.

In Figure 7 (a) shows the ground truth labels (i.e. field based estimates of AGB), which were derived from the field measurements and a species-specific allometric fit (i.e. Eq. 5). The central panel (b) shows the spatial distribution of residuals (i.e. $\epsilon = AGB_{ground-truth} - AGB_{prediction}$) of the AdaBoost context-aware regression results. The mean values converge towards zero (i.e. $\bar{\epsilon}_{SP} = 3.8$ kg, $\bar{\epsilon}_{CP} = -3.2$ kg), while the spread of the error distribution varies between SP and CP-datasets (i.e. $\sigma(\epsilon_{SP}) = 123$ kg, $\sigma(\epsilon_{CP}) = 140$ kg).

In Figure 7 (b) we visualized the lack of high spatial autocorrelation of errors (i.e. low clustering of errors), indicating that predictions are not geographically biased. Figure 7, panel c, displays the error distributions in both datasets. SP-errors show a unimodal distribution with a slight overestimation of DBH of -28 mm. CP-errors present a similar overestimation bias (-25 mm) with a bimodal distribution (the second mode is located at 25 mm of underestimation). The second mode of the bimodal pattern in the CP-dataset may correspond to the more frequent occurrence of larger trees, which tend to be underestimated (Figure 7, c, lower panels). It can be observed that, generally, smaller and thinner trees tend to be slightly overestimated (i.e. in the first two quantiles) compared to the largest trees, which tend to be underestimated.

Figure 8 presents the analysis of the relative importance of all predictors considered in the context-aware DBH regression with the AdaBoost regression model (i.e. the best performing one). The analysis reveals that in both SP- and CP-datasets, the most important context-based predictors are the average heights of the 5, 10, and 15 nearest neighboring trees, outperforming some individual-tree metrics, such as the crown metrics.

TWI made a marginal contribution to enhanced predictions, which was less than that of any neighborhood met-

ric. Moreover, although modest, TWI exhibited a greater impact on improved predictive performance at finer spatial resolutions in both datasets (Figure 8), whereas its contribution decreased at coarser resolutions (e.g. it did not significantly contribute as a predictor at 10m² resolution). This observation may indicate that the spatial resolution at which TWI is most informative of individual tree height, is similar to the usual tree crown size (i.e. 2-5 m² resolution), while at a coarser spatial resolution its contribution as predictor becomes negligible.

TABLE 1 Results (on test set) of the sampling plot (SP) dataset. Predictor variables are LiDAR-derived features; target variable is diameter at breast-height (DBH, in mm). The values are presented as mean \pm standard deviation of the 10 outer CV folds of the nested scheme. One asterisk (*) marks results where the enhancement introduced by context-awareness is statistically significant with "small" size effect, while ** and *** mark "medium" and "large" size effect, respectively. The best results are shown in bold.

Regression model	R ²	RMSE (mm)	MAE (mm)	MAPE (%)
AdaBoost (unaware)	0.830 \pm 0.05	58.0 \pm 9.0	43.3 \pm 4.4	19.1 \pm 1.9
AdaBoost (aware)	0.860 \pm 0.03 ***	52.7 \pm 5.3 ***	41.0 \pm 3.1 **	19.5 \pm 1.7
Random Forest (unaware)	0.818 \pm 0.04	60.2 \pm 7.3	46.8 \pm 4.5	22.8 \pm 5.8
Random Forest (aware)	0.838 \pm 0.05 *	56.5 \pm 9.2 *	41.6 \pm 5.4 ***	22.4 \pm 5.1
Lasso (unaware)	0.851 \pm 0.02	54.6 \pm 4.9	4.20 \pm 3.3	19.1 \pm 1.4
Lasso (aware)	0.852 \pm 0.02	54.4 \pm 4.9	4.17 \pm 3.5	18.8 \pm 1.7

TABLE 2 Results (on test set) of the control plot (CP) dataset. The predictive variables are LiDAR-derived features; the target variable is diameter at breast-height (DBH, in mm). The values are presented as mean \pm standard deviation of the 10 outer CV folds of the nested scheme. One asterisk (*) marks results where the enhancement introduced by context-awareness is statistically significant with "small" size effect. The best results are shown in bold.

Regression model	R ²	RMSE (mm)	MAE (mm)	MAPE (%)
AdaBoost (unaware)	0.713 \pm 0.07	54.7 \pm 5.98	43.0 \pm 5.26	15.5 \pm 2.4
AdaBoost (aware)	0.737 \pm 0.05 *	52.9 \pm 5.28 *	42.2 \pm 4.43 *	15.7 \pm 3.1
Random Forest (unaware)	0.688 \pm 0.07	57.0 \pm 5.9	43.8 \pm 5.1	15.7 \pm 3.1
Random Forest (aware)	0.705 \pm 0.04	55.6 \pm 5.3	41.3 \pm 5.5 *	15.9 \pm 4.3
Lasso (unaware)	0.741 \pm 0.09	51.3 \pm 6.6	39.1 \pm 5.2	13.6 \pm 1.6
Lasso (aware)	0.750 \pm 0.08	50.4 \pm 5.9	38.6 \pm 4.1	13.6 \pm 1.1

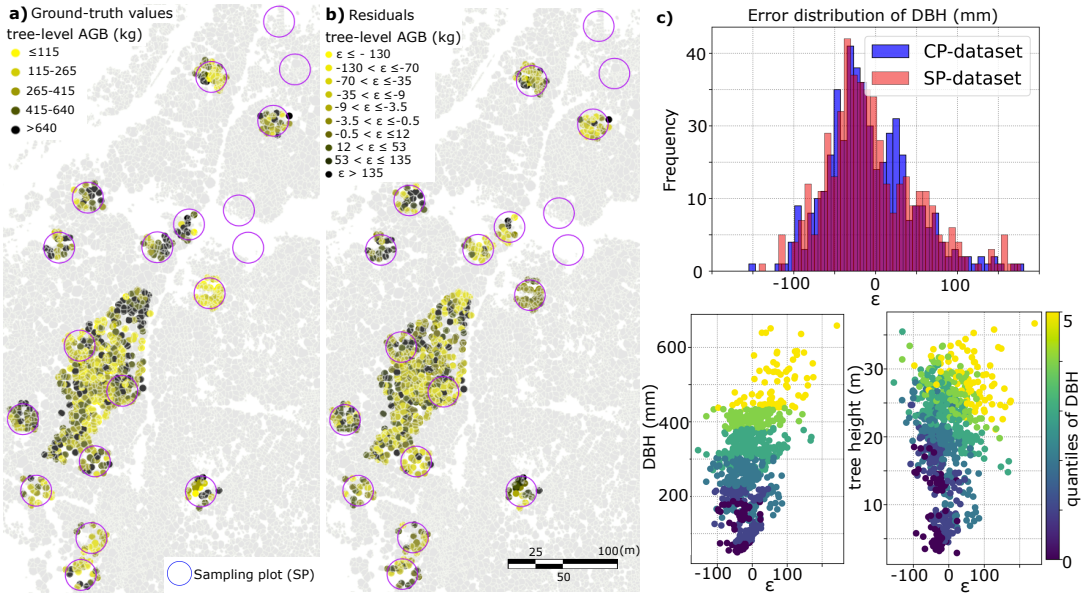


FIGURE 7 a: Spatial distribution of tree-level aboveground biomass (AGB) according to ground truth measurements (provided by the tree-monitoring campaigns of ICOS [44] and WSL [41]) and Eq. 5, grouped by quantiles. b: Spatial distribution of residuals ($\epsilon = AGB_{ground-truth} - AGB_{prediction}$) of AGB predictions with AdaBoost context-aware regression, grouped by quantiles. Negative values indicate overestimation. The four empty SP-plots (and the southernmost one not included) correspond to areas where the quality of the UAV LiDAR data collection was compromised; in such five plots, due to high level of noise in the point cloud data, all data was rejected (see Supporting Information, Annex V). c: error distributions of diameter at breast-height (DBH) in sampling plot (SP) and control plot (CP) datasets. The two bottom-right panels show the error distribution of DBH (in x-axis) vs. field-measurements of DBH and tree height. Colors representing quantiles do not entirely show a sharp separation (especially below 200 mm of DBH) because the quantiles refer to each dataset separately, which are differently distributed, as it is shown in Annex IV. For clarity, we opted to present all available data together, encompassing both datasets.

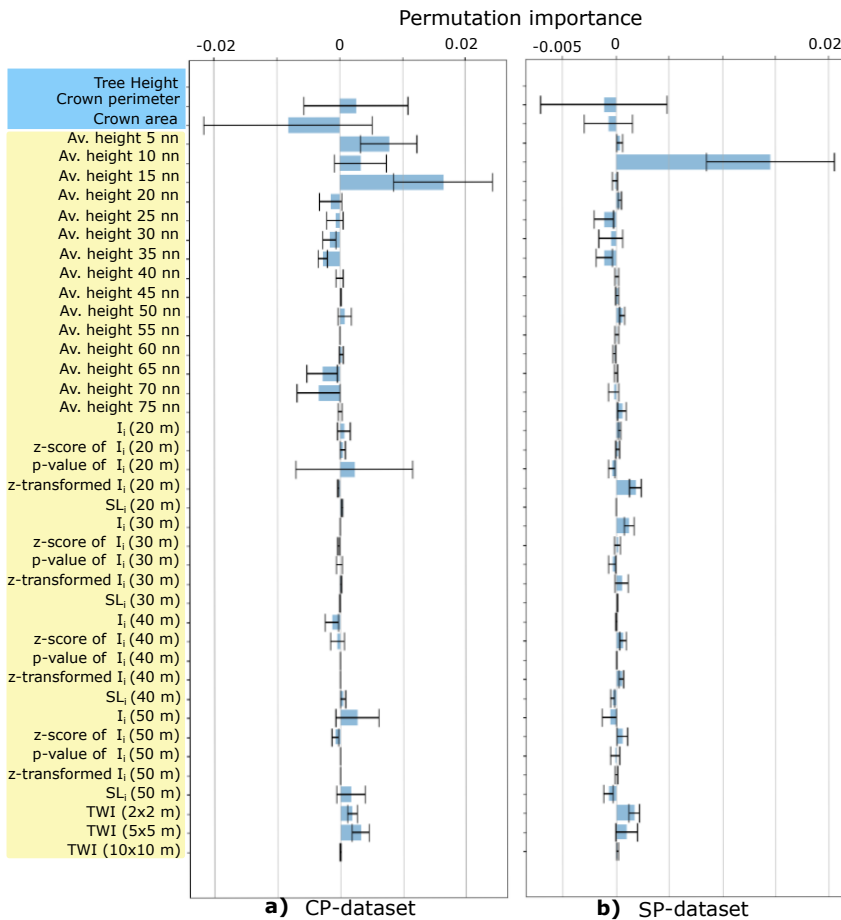


FIGURE 8 Inspection of predictors' importance via the permutation method [84] in the AdaBoost regression experiment in context-aware conditions. The left panel (a) shows results in the control plot (CP) dataset, and the right panel (b) shows results in the sampling plot (SP) dataset. Bar length and error bar show the mean and standard deviation of a predictor's importance, respectively. A negative mean value indicates that a predictor is less useful than when being randomly shuffled, so it lowers the model's predictive performance. Predictors highlighted in blue are individual tree traits; predictors highlighted in yellow are context-based (i.e. either neighborhood metrics or TWI). In both datasets, it can be noted how the average heights of the nearest 5-10 neighbors (nn) stand out as the strongest predictors, outperforming crown perimeter and crown area. In both plots (a and b), individual tree height (with importance: 0.85 in CP-trees; 1.3 in SP-trees) has been removed to facilitate visual comparison of the remaining predictors.

4 | DISCUSSION

4.1 | Enhancement of Tree-Level AGB Prediction

This study presents a method to enhance tree-level AGB estimates in Norway spruce forests using UAV LiDAR surveying and context-aware ML regression methods, in line with established context learning literature [31, 32, 33, 34, 35, 36, 37], and forest research—namely, NLME methods [13, 14, 15] and competition-based studies [16, 17, 18]. We further extend this approach to a fully integrated UAV LiDAR framework. The pairwise comparison of models consistently showed that context-aware regressions outperformed context-unaware regressions across models (except for Lasso in the SP-dataset, where performance stagnated), and in no case adding context information became detrimental. This finding may indicate that gradients in tree heights across the ecosystem proxy for hidden environmental and biotic mechanisms (e.g. windstorm disturbance, nutrient and soil moisture abundance, light harvesting competition) [99, 100] that influence tree growth, and can therefore be leveraged to enhance predictions of AGB at the single tree level. The results showed a consistently improved performance in AGB prediction when including context. The improvements were tested as statistically significant in four of the six pairwise experiments, with size effect ranging from small to large (Tables 1 and 2).

The accuracy enhancement gained from including context-aware features in the regression experiments varied between the two datasets considered (i.e. SP-trees and CP-trees). Context-aware regressions of DBH in SP-trees experienced greater enhancement than in CP-trees. This is consistent with the fact that the CP-dataset contains less variability of context, since it is a locally clustered and more homogeneous dataset, while the SP-dataset includes more variability in context features (Figure 2, b). The Norway investigated spruce forest presents a heterogeneous landscape, where the distribution of tree heights varies in space. Hence, the UAV LiDAR survey gives rise to a non-stationary dataset [59], showing both smooth gradients and sharp changes in height values, a non-trivial question in tree-phenotyping and functional trait mapping [31]. As SP-trees are grouped in scattered plots across the forest, their spatial distribution spans hundreds of meters, making them subject to a more diverse context than the very local CP-dataset.

We note that these findings are specific to the mountainous Norway spruce forest under investigation. Caution is advised when contemplating a direct application of this approach to more complex canopy structures and terrains, such as those found in deciduous, multilayered or broadleaf forests.

4.2 | The Role of Neighboring Context in AGB Prediction Performance

Most regression models achieved enhanced predictions when contextual information was included, with results consistently showing no deterioration. Thereby, the degree of local similarity of tree height (i.e. SL_i , local Moran's I_i) was most important and, to a lesser extent, the LiDAR-based TWI, indicating that although TWI is a good predictor of tree growth [67], the neighborhood information resulted more significant, in agreement with previous literature [20]. Conversely, including features informing about neighbor dissimilarity, such as local outliers of tree height detected using Local Outlier Factor [56] and Isolation Forest [57] algorithms did not result in enhanced predictions. We hypothesize that metrics containing information about the degree of local similarity may reveal the combined effect of ecological processes that are specific to the immediate neighboring context. Conversely, metrics containing information of the dissimilarities of the individual trees do not help to uncover such processes, although they remain useful in detecting outstanding trees (i.e. local outliers).

Context-based features at closer distances generally showed larger predictive power but also larger variance (as

less neighboring trees are computed), therefore producing a strong and fluctuating signal, that in some cases was challenging for the ML model to incorporate in the learning process. For instance, the p-value of Local Moran's I_i at a 20m range in the CP-dataset has an average positive effect but is not a stable predictor (Figure 8, a). This can be observed in the general trend of larger standard deviations in the permutation importance of predictors retrieved at short ranges than at greater distances (Figure 8). After the peak in the spatial autocorrelation of tree height (i.e. at larger distance bands than 40m), the significance of clustering of tree height values declined, presenting another shoulder at a distance of 110m (Figure 4, b). As the neighborhood size increased beyond the 40-meter distance range, the predictive power of the metrics derived from the neighboring trees (i.e. the influence of local context) progressively smoothed down [64].

In accordance with competition-based studies [16, 17, 18], we observe that the strongest context-based predictors are those retrieved from the immediate neighboring trees in both datasets, i.e. the average height of 5, 10 and 15 nearest neighbors (Figure 8). However, our method additionally allows to compare the relative importance of competition-derived metrics and other context-based metrics operating at larger scales. For instance, in Figure 8 (a) it is shown that local Moran's I_i retrieved at a 50 m range is comparable in importance to the average height of the closest 10 neighboring trees.

A general difference observed between the CP and the SP-datasets is that the predictors' importances in the CP-dataset fluctuate more (i.e. larger standard deviations). Further, in the SP-dataset, predictors rarely become negative and if they do, it is to a lesser extent. Given its broader spatial distribution and greater contextual variability, we regard the SP-dataset as a more representative sample of the entire forest population compared to the clustered CP-dataset. Consequently, the finding that context-based features demonstrate greater stability within the SP-dataset is noteworthy.

Including morphometric variables calculated from the tree assemblages in the regression experiments did not result in improved predictions of DBH and therefore were not included in the final modelling of DBH. However, the analysis of shapes of the tree assemblages revealed a convergence assembly pattern of tree heights [101], which was specially remarkable in certain metrics, which showed a strong correlation with tree height (e.g. concavity [70] and length-to-width ratio [87]), as discussed in Section 4.3. Nevertheless, none of the morphometric variables obtained from the tree assemblage analysis proved useful to improve predictions of DBH.

Considering context metrics to enhance estimates of DBH at the individual tree level in coniferous forests has previously been suggested in seminal works [22, 102] and been adopted subsequently for various applications in forest research [21, 23]. E.g. Lo and Lin (2012) [18] proposed a competition-specific index to capture the effect of the competing pressure of immediate neighbors. Moreover, recent investigations on tree morphology and productivity in coniferous forests [16, 17] have motivated the further development of competition-aware approaches to improve the prediction accuracy of individual tree traits, e.g. diameter growth, leveraging tree canopy metrics. Such approaches focused on canopy metrics encourage the potential applicability in fully integrated UAV LiDAR frameworks.

In forest biomass research, a commonly recognized approach is calibrating regression models with plot-level metrics for predicting tree-level structural traits (e.g. plot-level random effects in NLME methods), which has been pointed out as a methodological limitation [20]. Indeed, the results of such approaches are constrained by the artificially-delineated plot size, and it has been observed that accuracy increases with a progressively larger plot size [13, 15]. Furthermore, how diverse context-based attributes retrieved at different distance ranges affect tree-level predictions had not been investigated before. In this regard, our results show that the variability and extent of context determines its beneficial leverage for prediction of tree-level traits (e.g. DBH, AGB).

This study continues this line of work and sheds light on how the local spatial context can be defined and leveraged in tree-level structural trait predictions (i.e. DBH), making a case for AGB estimates in a Norway spruce forest. The

analysis shows that there is an optimal range to computing neighborhood metrics. In the study case considered here, this corresponded to a 40 m range distance, based on the spatial autocorrelation of tree heights. Further, we found that the predictive power of context-based metrics is sensitive to context extent (i.e. the range at which such metrics are calculated). This observation may indicate that defining context based on plot-level metrics retrieved from artificially bounded units [13, 14, 15] may be seen as a constrained approach, as observed previously [20, 103]. Likewise, in the light of this observation, and in line with recent studies [104], determining the significant contextual extent of individual functional traits based on units of fixed size (e.g. pixel size) appears to be a suboptimal technique. Therefore, future forest research would probably benefit from including context-awareness determined by spatial association of tree traits, bearing in mind that context-detection is trait-dependent and may vary depending on dataset source—e.g. spatial autocorrelation as a function of distance (Figure 4) is sensitive to CHM segmentation quality—and method applied—e.g. delineation of tree assemblages varied slightly between local Moran's I_i , and SL_i , as we show in Figure 5.

The motivation for this study has been to introduce more quantifiable terms to ecological reasoning and to propose a standardized method of incorporating context-awareness into AGB research. The method proposed is conceived for a fully integrated UAV LiDAR framework. Since we do not make use of external data sources but, on the contrary, every predictor is native to the UAV LiDAR dataset, and we do not use understory vegetation metrics, the method may be readily tested in other coniferous forests.

Lastly, we note that optical RS studies usually define the optimal scale of analysis as a trade-off between the observational extent (i.e. area surveyed) and the unit resolution (i.e. pixel size) [104, 105]. Also, in ecological research, it is common to subsample datasets using natural subregions based on ancillary ecological criteria (e.g. ecoregions, conservation status) [106]. Conversely, here we defined the range of influence of context-based metrics (i.e. the extent of tree neighborhoods) using a dataset-native approach, based entirely on the spatial association of individual tree heights. This permitted us to determine the context of influence unhampered by the RS technique and not using external data sources. In computer vision studies that investigate contextual learning, image analyses typically do not assume a specific optimal scale [107, 108], such as in geographic analysis [109]. In this study, local context was defined based on the spatial association of a real physical attribute of the target objects (i.e. tree heights), and not defined by an artificially bounded unit (e.g. pixel size or plot size) so that the resulting distance could be considered characteristic of the forest ecosystem.

4.3 | Tree Assemblages

The quantitative comparison of morphometric variables between tree assemblages (Figure 6) permitted to examine whether trees—grouped by local association of tree height—persistently show different shapes at the group level, shedding light on the relationship between context-based traits (e.g. concavity of a tree assemblage) and LiDAR-derived tree height. Remarkably, it was observed that tree assemblages delineated according to the spatial lag of tree height (i.e. SL_i) presented clear positive correlations with two-dimensional morphometric features at the tree assemblage level.

For instance, assemblages with higher trees (i.e. labeled as *Highest* according to SL_i , or *High-High* according to local Moran's I_i) are consistently rounder, larger and more regular in shape. As visualized in Figure 6, SL_i correlates positively with shape regularity [89], two-dimensional concavity [70], length-to-width ratio [87] and size, indicating a consistent trait-convergence assembly pattern [101]. Higher trees seem to converge in most sheltered areas (i.e. thalwegs and local sub-basins) so that tree assemblages with highest SL_i tend to adopt the morphological features of the drainage network's shape (see Figure 9, in Annex I). Interpretation of this observation would go beyond the scope

of this study. However, it may indicate that both the shape and location of tree assemblages of different heights are conditioned by underlying environmental and biotic driving mechanisms.

In the coniferous forest studied here, a significant degree of clustering of tree heights takes place (Figure 5, a), while spatial gradients of tree height present preferential shapes and directions (Figure 5, b). These observations indicate that there is tree-height convergence and a tendency toward optimal phenotype expression (i.e. maximum growth performance) around the runoff drainage network (Figure 9, c, in Annex I). Higher trees are found in sheltered regions and concave channels—which generally benefit from more frequent runoff events and deeper soils [110, 111]. This may indicate that favorable environmental conditions (e.g. deeper soil, lower soil moisture recession rates, greater availability of soil nutrients due to leaching) allow individuals to reach their optimal phenotype. Conversely, a lower SL_i of tree height in more exposed terrain (e.g. ridges, hilltops) indicates that environmental filtering (e.g. windstorm disturbance) or a reduced competition in light harvesting could play a significant role in determining the location of low SL_i tree assemblages (Figure 9, a, in Annex I). Thus, the relatively reduced tree height in exposed areas could indicate a passive response of tree height to harsher environmental conditions [112], an active response to higher light availability [99] or a limitation to tree growth caused by other local factors, such as lower soil depth or nutrients availability [1, 111]. Nevertheless, this study cannot provide an interpretation of such observations, as shifts in the variance of functional traits across environmental gradients (i.e. spatial patterns of trait similarity) do not bring strong evidence of either biotic or environmental filtering on their own [113].

4.4 | Methods Applied

We have aimed at preserving a fully-native LiDAR approach, so that the applicability of the method proposed is not compromised by lacking local ancillary data, which may become a limiting factor in forest monitoring. However, one main methodological constraint we acknowledge is that the strength of our results is currently limited by the lack of replicates at different forest sites, so that we cannot yet confirm these findings to be generally applicable to a wider range of forest types beyond mountainous Norway spruce forests. Nevertheless, the enhancement in predictions was observed across most models and in two separate datasets. Furthermore, we note that the pre-processing tasks (marked * in Figure 3, explained Section 2.3) required as part of the experimental design, simplifies the actual PCD scene representing the forest scenario, hampering a fully-automated, streamlined application, and case-specific considerations are still required. In sum, further research would be needed to evaluate the transferability of the method and compare these results across various tree species and stand configurations.

A more general caveat, but equally important w.r.t. results, lies on the fact of normalizing the CHM to derive individual tree height. In very steep slopes, CHM accuracy can be compromised, therefore affecting AGB estimation results.

5 | CONCLUSIONS

This study introduces and evaluates a fully integrated UAV LiDAR method that utilizes context information to improve the accuracy of AGB estimates of individual trees, making a case for a coniferous forest. The performance of the regression models consistently demonstrated improvements in AGB prediction when incorporating context-aware features. The exception was the Lasso model, which stagnated in the SP-dataset. Importantly, in no case did contextual features have a detrimental effect. We conclude from our results that the use of context-aware features as predicting variables can substantially improve estimates of AGB in coniferous forests—i.e. the best performing model

599 showed a reduction of RMSE of 9.1 % and 4.0 %, and an increase in R^2 by 3.5 % and 3.2 %, in the SP- and CP-datasets,
600 respectively. The different degree of enhancement in model performance between the two datasets is considered
601 to be related to the contrasting variability in context between the CP-dataset (clustered and continuous) and the SP-
602 dataset (discontinuous and scattered in twenty different plots across the study site). Features that provide information
603 about the tree neighborhood (e.g. SL_i of tree height, average height of k -nearest trees) contain useful information
604 to improve predictions of different individual tree traits (e.g. DBH, AGB). This finding suggests that the information
605 retrieved from the local context serves as a proxy for underlying ecological mechanisms that exert influence on the
606 individual tree AGB as a result of local adaptations to environmental and biotic processes.

607
608 We conclude that the proposed fully native UAV LiDAR approach, which integrates spatial associations of tree
609 heights, is more efficient in incorporating context compared to methods constrained by the use of data collected in
610 artificially delineated monitoring plots. This is because at larger scales beyond the plot level, contextual features might
611 play a role in improving AGB predictions. Moreover, as the method proposed uses metrics entirely native to the UAV
612 LiDAR dataset, it does not rely on tailored process-specific indices (e.g. competition metrics) or ancillary data sources
613 (e.g. biome type, conservation status, ecoregions).

614 Author contributions

615 Original conceptual framework: JCR and SO; experimental design: JCR; UAV-LiDAR data collection: JCR; field-based
616 data provision and curation: FS and MG; laser data pre- and postprocessing: JCR; feature engineering, training and
617 evaluation of the machine learning models: JCR and SO; visualisation: JCR; supervision: AD, KT and FG; project
618 administration: AD, NB, KT, FG and JCR; writing—original draft preparation: JCR; writing—review and editing: SO,
619 MG, FS, FG, KT, NB, AD and JCR.

620 All authors have read and agreed to the published version of the manuscript.

621 Acknowledgements

622 Helpful discussions with Thomas Friborg, Daniel Kükenbrink and Moritz Bruggisser are gratefully acknowledged. Like-
623 wise, we acknowledge the contribution of the field workers, who are responsible for collecting the forest inventory
624 data on a regular basis, used here as ground truth.

625 Funding

626 This project received funding support from the Talent Program Horizon 2020/Marie Skłodowska-Curie Actions, a
627 Villum Experiment grant by the Velux Foundations, DK (MapCland project, number: 00028314), and the DeepCrop
628 project (UCPH Strategic plan 2023 Data + Pool). MG also acknowledges funding by Swiss National Science Foundation
629 project ICOS-CH Phase 3 (20F120_1982287).

630 Data availability

631 The code, data and metadata that support the findings of this study are available from the corresponding author,
632 JCR, upon responsible request, and will be published in a DOI-compliant public repository upon acceptance of this
633 manuscript.

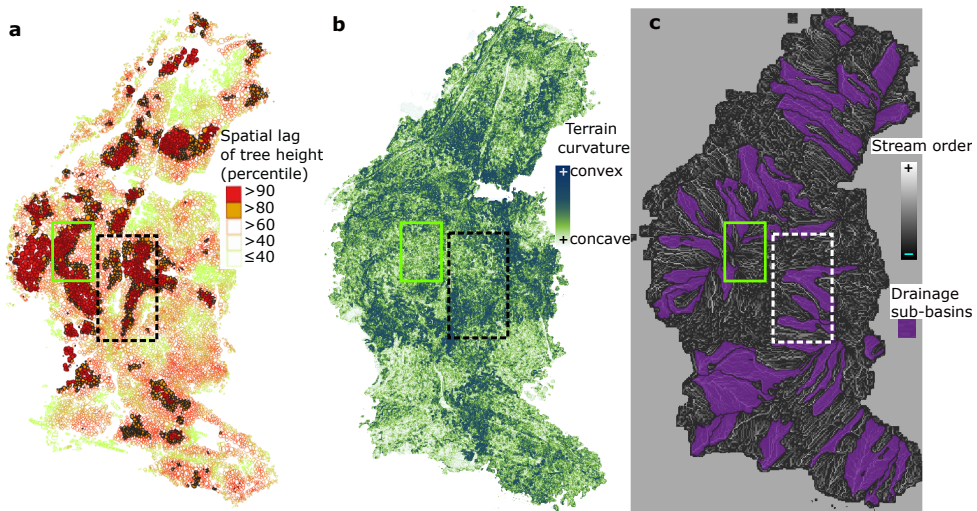


FIGURE 9 a: Spatial lag of tree height derived from the individual tree crown (ITC) polygon dataset. b: Map of terrain curvature derived from point cloud data (PCD) ground-returns. c: Hydrological network (Strahler's stream order) [114]. In all three panels, the dashed box indicates an area favored by surface hydrological conditions, hosting an assemblage of trees in the >90 % percentile of spatial lag of tree height. The solid green box indicates an area at a hilltop, unfavored by surface hydrological processes, more exposed to windstorm disturbance, and hosting an assemblage of trees in the < 60% percentile of spatial lag of tree height.

634 Supporting Information

635 | Annex I: Location and Morphometry of Tree Assemblages

636 The spatial distribution of SL_i presents directional anisotropy, stretching across preferential areas which seem to
 637 match sheltered sectors of the forest, such as concave thalwegs. Figure 9 highlights two neighboring areas with
 638 contrasting values of SL_i , indicating that surface hydrology processes and terrain exposure (i.e. terrain convexity)
 639 condition tree growth at the group level.

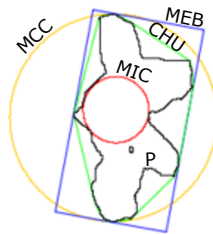


FIGURE 10 Calculation of elementary geometries fitted to an exemplary tree assemblage. P: polygon of tree assemblage (black line). MCC: minimum circumscribed circle (in green). MIC: maximum inscribed circle (in red). CHU: convex hull (in yellow). MEB: minimum enclosing box containing P (in blue).

640 The morphometric analysis was conducted by taking into account the outer borders of tree assemblages defined
 641 either by SL_i , or by local Moran's I_i (delineated as explained in Section 2.3; results shown in Figure 5). The 20 basic

642 morphometric variables (Table 3) result from fitting elementary geometries to the tree assemblage polygon. The 20
 643 derived variables (Table 4) are adimensional parameters (except for concavity, in m^2) obtained by combining the basic
 644 parameters.

TABLE 3 Twenty basic morphometric variables derived from the tree assemblage polygon dataset (as described in Güler et al., 2021) [71]. P: polygon of a tree assemblage.

Basic parameters	Description	units
XPOL	Easting of P centroid	m
YPOL	Northing of P centroid	m
APOL	Area of P	m^2
PPOL	Perimeter of P	m
LPOL	Major axis' length of P	m
WPOL	Minor axis' length of P	m
N-S	North-South alignment of P, defined as $ \sin(\text{azimuth}) $ of major axis	\emptyset
AFOB	Area of the bounding box fully containing P	m^2
PFOB	Perimeter of the bounding box fully containing P	m
AMEB	Area of minimum enclosing box	m^2
PMEB	Perimeter of minimum enclosing box	m
ACHU	Area of the convex hull fully containing P	m^2
PCHU	Perimeter of the convex hull fully containing P	m
AMCC	Area of the minimum circumscribed circle enclosing P	m^2
PMCC	Perimeter of the minimum circumscribed circle enclosing P	m
RMCC	Radius of the minimum circumscribed circle enclosing P	m
AMIC	Area of the maximum inscribed circle enclosing P	m^2
PMIC	Perimeter of the maximum inscribed circle enclosing P	m
RMIC	Radius of the maximum inscribed circle enclosing P	m

TABLE 4 20 morphometric variables derived from the tree assemblage polygon dataset (as described in [71]). P: tree assemblage polygon. A: area of P. L: length of major axis of P. W: width of minor axis of P (i.e. width). ACHU: area of convex hull fully containing P. RMCC: radius of minimum circumscribed circle. PCHU: perimeter of convex hull fully containing P. AMEB: area of minimum enclosing box.

Derived parameters	Name	Definition	Source
LTWR	Length-to-width ratio	L/W	[87]
WTLR	Width-to-Length ratio	W/L	[88]
ELLF	Ellipticity Factor	$ L - W /(L + W)$	[89]
CIRR	Circularity Ratio	P^2/A	[90]
ZFOR	Zăvoianu's Form Factor	$(16A)/P^2$	[91]
COMF	Compactness Factor	$P/(4\pi A)^{0.5}$	[71]
MCIR	Miller's Circularity Ratio	$(4\pi A)/P^2$	[92]
DISM	Dispersion Measure	$1 - [(4\pi A)^{0.5}/P]$	[90]
COMI	Complexity Index	$1 - [(4\pi A)/P^2]$	[71]
HFOR	Horton's Form Factor	A/L^2	[87]
ELOF	Elongation Factor	$(4A/\pi)^{0.5}/L$	[93]
LEMUR	Lemniscate Ratio	$(\pi L^2)/4A$	[94]
REGF	Regularity Factor	$(\pi LW)/4A$	[89]
SHAF	Shape Factor	$[(4\pi A)/P^2] \times (L/W)$	[89]
CONV	Convexity	$PCHU/P$	[95]
CONC	Concavity	$ACHU - A$	[70]
SOLI	Solidity	$A/ACHU$	[96]
RECT	Rectangularity	$A/AMEB$	[97]
ROUN	Roundness	$(4\pi A)/(PCHU)^2$	[95]
SPHE	Sphericity	$(4A/\pi)^{0.5}/(2 \times RMCC)$	[98]

Annex II: Context Detection

The distance range selected around each tree to compute neighborhood metrics (i.e. context detection), was conducted based on the peak of significance (determined using the standard z-score) of local spatial autocorrelation (using Local Moran's I_i) as function of increasing distance, in steps of 10 m.

Local Moran's I_i is a spatial statistic that relates attribute similarity to locational similarity, mapping the autocorrelation of individual tree heights across the geographical space, as defined above (Eq. 1, in Section 3.1). The expression below (Eq. 6) defines the z-score, which is used to measure the significance of tree-height clustering. Z-scores shows the significance of the clustering by subtracting the observed I_i values from the expectation (i.e. $E[I_i]$), and normalizing over the standard deviation of I_i . This produces a distance metric in units of standard deviations. $E[I_i]$ is the expected value of local Moran's I_i under the null hypothesis of no spatial autocorrelation.

$$z_{score} = \frac{I_i - E[I_i]}{\sqrt{V[I_i]}}, \quad (6)$$

Neighborhood size was determined according to the significance of spatial autocorrelation (defined as local Moran's I_i) as function of distance, via the standard z-score. Z-score measures the distance of a measured value from the expectation in units of standard deviation, under the assumption of randomly distributed values.

and the expected value of Moran's I under the null hypothesis of no spatial autocorrelation is:

$$E[I_i] = -\frac{\sum_{j=1}^m w_{ij}}{m-1} = -\frac{1}{m-1}, \quad (7)$$

where m equals the total number of trees in the neighborhood. At large sample sizes (i.e. for increasing values of m), the expected value approaches zero. The spatial weights allocated to each neighboring tree j are standardized [65], such that for each tree i , $\sum_j w_{ij} = 1$. The variance of local Moran's I_i is defined as the expectation of the square of I_i , minus the square of the expectations of I_i :

$$V[I_i] = E[I_i^2] - E[I_i]^2, \quad (8)$$

Annex III: Training, Validation and Test of results

664

665

666

667

668

669

670

671

672

Nested cross-validation (NCV) [83] follows the updated and established recommendations to achieve an unbiased estimate of the generalization error, while making optimal use of the limited available data. It is an evaluation method for determining the accuracy of point estimates and confidence intervals for prediction errors. As a modification developed from standard cross-validation [115], NCV improves estimates of prediction accuracy and confidence intervals by accounting for the correlation between error estimates in different folds, an inconvenient phenomenon affecting standard cross-validation that may render error estimates overly optimistic. How NCV is implemented is shown in Figure 11. The entire algorithmic routine of NCV is presented immediately below. The input data (i.e. X, Y) corresponds to the set of predictors (i.e. X), and the target variable DBH (i.e. Y), respectively.

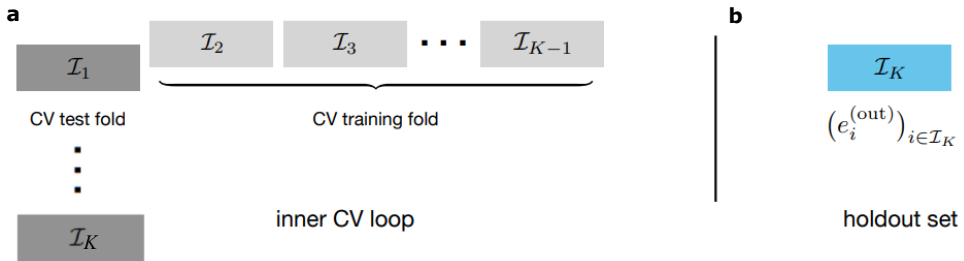


FIGURE 11 Visualization of 10-fold nested cross-validation (CV). **a:** at each of the K steps ($K = 10$), we perform standard cross-validation for model training (light grey folds), holding one of the folds out of the inner CV loop (dark grey fold). **b:** The fresh holdout folds (in blue) are never used for hyperparameter optimization or feature selection (figure adapted from Bates et al., 2021 [83]).

Algorithm 1: Nested cross-validation

Input: data (X, Y) , fitting algorithm A , loss function l , number of folds K , number of repetitions R

```

procedure Nested cross-validation  $(X, Y)$            // ▷ primary algorithm;
   $es \leftarrow []$                                    // ▷ initialize empty vectors;
   $a\_list \leftarrow []$                                // ▷ (a) terms;
   $b\_list \leftarrow []$                                // ▷ (b) terms;
  for  $r \in \{1, \dots, R\}$  do
    Randomly assign points to folds  $I_1, \dots, I_K$ ;
    for  $k \in \{1, \dots, K\}$  do
      // ▷ outer CV loop;
       $e^{(in)} \leftarrow$  inner cross-validation  $(X, Y, \{I_1, \dots, I_K\} \setminus I_k)$  // ▷ inner CV loop;
       $\hat{\theta} \leftarrow A((X_i, Y_i)_{i \in I \setminus I_k})$ ;
       $e^{(out)} \leftarrow (l(\hat{f}(X_i, \hat{\theta}), Y_i))_{i \in I_k}$ ;
       $b\_list \leftarrow$  append( $a\_list, (mean(e^{(in)}) - mean(e^{(out)}))^2$ );
       $b\_list \leftarrow$  append( $b\_list, var(e^{(out)})/|I_k|$ );
       $es \leftarrow$  append( $es, e^{(in)}$ );
       $\overline{MSE} \leftarrow mean(a\_list) - mean(b\_list)$ ;
       $\overline{Err}^{(NCV)} \leftarrow mean(es)$ ;
      return:  $(\overline{Err}^{(NCV)}, \overline{MSE})$  // ▷ prediction error estimate and MSE estimate;

procedure Inner cross-validation  $(X, Y, \{I_1, \dots, I_{K-1}\})$  // ▷ inner cross-validation subroutine;
   $e^{(in)} \leftarrow []$ ;
  for  $k \in \{1, \dots, K-1\}$  do
     $\hat{\theta} \leftarrow A((X_i, Y_i)_{i \in I_i \cup \dots \cup I_{K-1} \setminus I_k})$ ;
     $e^{(temp)} \leftarrow (l(\hat{f}(X_i, \hat{\theta}), Y_i))_{i \in I_k}$ ;
     $e^{(in)} \leftarrow$  append( $e^{(in)}, e^{(temp)}$ );
  return:  $e^{(in)}$ ;

```

Output: Nested cross-validation (X, Y)

Annex IV: Distribution Shift Between CP-trees and SP-trees

673

674 By morphological tree traits, we refer to the structural tree parameters considered in the study (i.e. tree height and
675 DBH). Here below, we visualize the joint distributions of DBH and tree height in the two datasets considered in order
676 to highlight how differently distributed they are.

677

678 The joint distributions of morphological tree traits DBH and tree height in both CP and SP-datasets show a shift
679 between the two [82]. For instance, the kernel probability distribution of heights shows that the SP-dataset contains
680 a higher amount of short trees (i.e. heights $\in (3, \dots, 8)$ m), that cover a wide range of DBH values. Also, the range of
681 DBH is broader in the SP-dataset compared to the CP-dataset, and the instances do not exhibit an accumulation in
682 the center as evident as the one observed in the CP-dataset.

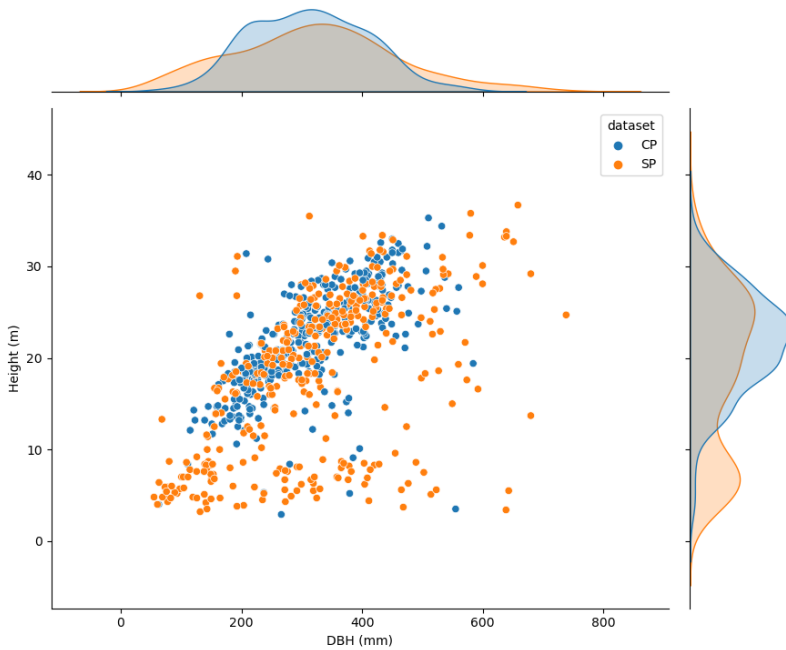


FIGURE 12 Joint distributions of diameter at breast-height (DBH) and tree height from field-based inventory data. It should be noted that the two datasets are differently distributed—i.e. there is a dataset shift [82] between sampling plots (SP) and control plots (CP) datasets.

683

Annex V: Elevation map of the study site

684

685

686

687

688

689

We provide the digital elevation model of the study area (Figure 13, a) to understand differences in flight heights (Figure 2) and to complement the information given on terrain exposure and surface hydrology (Figure 9). Figure 13, (b) shows the five rejected SP-plots and one valid (i.e. SP-18), for comparison. Among the rejected SP-plots, 1, 2, 9 and 10 show an insufficiently descriptive CHM, while SP-14 shows an intractable allocation of ground-based labels. All five rejected SP-plots were discarded before starting the modelling process, so they did not take part in the regression experiments.

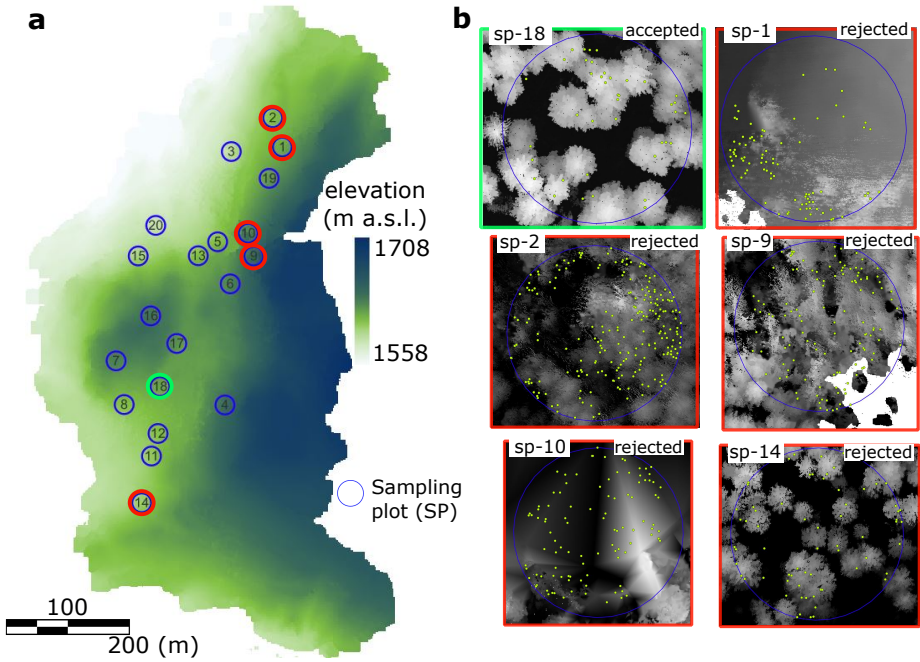


FIGURE 13 a: Digital elevation model of the stud area. a.s.l.: elevation above sea level, in m. The blue circles represent the SP-plots, numbered by their ID code (1-20). The green and red circles refer to the plots shown in panel b. b: Five SP-plots rejected and one valid (SP-18) given for comparison of contrasting quality of canopy height models, derived from the UAV LiDAR point cloud data. In all six SP-plots, the yellow dots indicate the location of tree stems according to the field-based inventory.

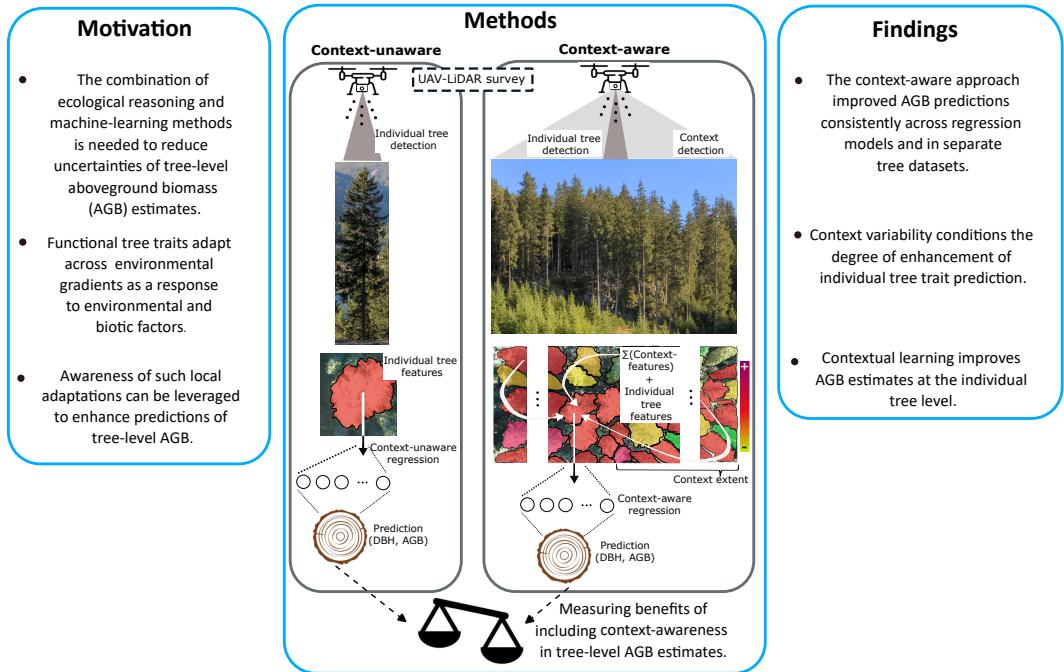
690 **Graphical Abstract**

FIGURE 14 Graphical Abstract of the study.

691 **References**

- 692 [1] Fatichi S, Pappas C, Zscheischler J, Leuzinger S. Modelling carbon sources and sinks in terrestrial vegetation. *New*
 693 *Phytologist* 2019;221(2):652–668.
- 694 [2] Pörtner HO, Roberts DC, Adams H, Adler C, Aldunce P, Ali E, et al. *Climate change 2022: Impacts, adaptation and*
 695 *vulnerability*. IPCC Geneva, Switzerland; 2022.
- 696 [3] Gundersen P, Thybring EE, Nord-Larsen T, Vesterdal L, Nadelhoffer KJ, Johannsen VK. Old-growth forest carbon sinks
 697 overestimated. *Nature* 2021;591(7851):E21–E23.
- 698 [4] Friedlingstein P, Jones MW, O'sullivan M, Andrew RM, Hauck J, Peters GP, et al. Global carbon budget 2019. *Earth*
 699 *System Science Data* 2019;11(4):1783–1838.
- 700 [5] Baccini A, Walker W, Carvalho L, Farina M, Sulla-Menashe D, Houghton R. Tropical forests are a net carbon source
 701 based on aboveground measurements of gain and loss. *Science* 2017;358(6360):230–234.
- 702 [6] Duncanson L, Armston J, Disney M, Avitabile V, Barbier N, Calders K, et al. The importance of consistent global forest
 703 aboveground biomass product validation. *Surveys in geophysics* 2019;40:979–999.
- 704 [7] Santini F, Kefauver SC, Resco de Dios V, Arous JL, Voltas J. Using unmanned aerial vehicle-based multispectral, RGB
 705 and thermal imagery for phenotyping of forest genetic trials: A case study in *Pinus halepensis*. *Annals of Applied*
 706 *Biology* 2019;174(2):262–276.

- 707 [8] Yao W, Krull J, Krzystek P, Heurich M. Sensitivity analysis of 3D individual tree detection from LiDAR point clouds of
708 temperate forests. *Forests* 2014;5(6):1122–1142.
- 709 [9] Dalponte M, Coomes DA. Tree-centric mapping of forest carbon density from airborne laser scanning and hyperspectral
710 data. *Methods in ecology and evolution* 2016;7(10):1236–1245.
- 711 [10] Kükenbrink D, Hueni A, Schneider FD, Damm A, Gastellu-Etchegorry JP, Schaepman ME, et al. Mapping the irradiance
712 field of a single tree: Quantifying vegetation-induced adjacency effects. *IEEE Transactions on Geoscience and Remote
713 Sensing* 2019;57(7):4994–5011.
- 714 [11] Cabo C, Ordóñez C, López-Sánchez CA, Armesto J. Automatic dendrometry: Tree detection, tree height and diame-
715 ter estimation using terrestrial laser scanning. *International journal of applied earth observation and geoinformation*
716 2018;69:164–174.
- 717 [12] Kukkonen M, Maltamo M, Korhonen L, Packalen P. Multispectral airborne LiDAR data in the prediction of boreal tree
718 species composition. *IEEE Transactions on Geoscience and Remote Sensing* 2019;57(6):3462–3471.
- 719 [13] Hao Y, Widagdo FRA, Liu X, Quan Y, Dong L, Li F. Individual tree diameter estimation in small-scale forest inventory
720 using UAV laser scanning. *Remote Sensing* 2020;13(1):24.
- 721 [14] Yang Z, Liu Q, Luo P, Ye Q, Sharma RP, Duan G, et al. Nonlinear mixed-effects height to crown base model based on both
722 airborne LiDAR and field datasets for *Picea crassifolia* Kom trees in northwest China. *Forest Ecology and Management*
723 2020;474:118323.
- 724 [15] Liu X, Hao Y, Widagdo FRA, Xie L, Dong L, Li F. Predicting height to crown base of *Larix olgensis* in Northeast China
725 Using UAV-LiDAR data and nonlinear mixed effects models. *Remote Sensing* 2021;13(9):1834.
- 726 [16] Sun S, Cao QV, Cao T. Evaluation of distance-independent competition indices in predicting tree survival and diameter
727 growth. *Canadian Journal of Forest Research* 2019;49(5):440–446.
- 728 [17] Zhang B, Sajjad S, Chen K, Zhou L, Zhang Y, Yong KK, et al. Predicting tree height-diameter relationship from relative
729 competition levels using quantile regression models for Chinese fir (*Cunninghamia lanceolata*) in Fujian province, China.
730 *Forests* 2020;11(2):183.
- 731 [18] Lo CS, Lin C. Growth-competition-based stem diameter and volume modeling for tree-level forest inventory using
732 airborne LiDAR data. *IEEE Transactions on Geoscience and Remote Sensing* 2012;51(4):2216–2226.
- 733 [19] Potvin C, Dutilleul P. Neighborhood effects and size-asymmetric competition in a tree plantation varying in diversity.
734 *Ecology* 2009;90(2):321–327.
- 735 [20] Ratcliffe S, Holzwarth F, Nadrowski K, Levick S, Wirth C. Tree neighbourhood matters—Tree species composition drives
736 diversity–productivity patterns in a near-natural beech forest. *Forest Ecology and Management* 2015;335:225–234.
- 737 [21] Andersen HE, McGaughey RJ, Reutebuch SE. Estimating forest canopy fuel parameters using LIDAR data. *Remote
738 sensing of Environment* 2005;94(4):441–449.
- 739 [22] Næsset E, Økland T. Estimating tree height and tree crown properties using airborne scanning laser in a boreal nature
740 reserve. *Remote Sensing of Environment* 2002;79(1):105–115.
- 741 [23] Rijal B, Weiskittel AR, Kershaw Jr JA. Development of height to crown base models for thirteen tree species of the
742 North American Acadian Region. *The Forestry Chronicle* 2012;88(1):60–73.
- 743 [24] Antonio N, Tome M, Tome J, Soares P, Fontes L. Effect of tree, stand, and site variables on the allometry of *Eucalyptus
744 globulus* tree biomass. *Canadian Journal of Forest Research* 2007;37(5):895–906.

- 745 [25] Hyyppä E, Yu X, Kaartinen H, Hakala T, Kukko A, Vastaranta M, et al. Comparison of backpack, handheld, under-canopy
746 UAV, and above-canopy UAV laser scanning for field reference data collection in boreal forests. *Remote Sensing*
747 2020;12(20):3327.
- 748 [26] Li N, Ho CP, Xue J, Lim LW, Chen G, Fu YH, et al. A Progress Review on Solid-State LiDAR and Nanophotonics-Based
749 LiDAR Sensors. *Laser & Photonics Reviews* 2022;16(11):2100511.
- 750 [27] Oehmcke S, Li L, Revenga JC, Nord-Larsen T, Trepekli K, Gieseke F, et al. Deep learning based 3D point cloud regres-
751 sion for estimating forest biomass. In: *Proceedings of the 30th International Conference on Advances in Geographic*
752 *Information Systems*; 2022. p. 1–4.
- 753 [28] Réjou-Méchain M, Barbier N, Couteron P, Ploton P, Vincent G, Herold M, et al. Upscaling forest biomass from field to
754 satellite measurements: sources of errors and ways to reduce them. *Surveys in Geophysics* 2019;40(4):881–911.
- 755 [29] Xu D, Wang H, Xu W, Luan Z, Xu X. LiDAR applications to estimate forest biomass at individual tree scale: Opportunities,
756 challenges and future perspectives. *Forests* 2021;12(5):550.
- 757 [30] Biging GS, Dobbertin M. Evaluation of competition indices in individual tree growth models. *Forest science*
758 1995;41(2):360–377.
- 759 [31] Schiefer F, Kattenborn T, Frick A, Frey J, Schall P, Koch B, et al. Mapping forest tree species in high resolution UAV-based
760 RGB-imagery by means of convolutional neural networks. *ISPRS Journal of Photogrammetry and Remote Sensing*
761 2020;170:205–215.
- 762 [32] Marques O, Barenholtz E, Charvillat V. Context modeling in computer vision: techniques, implications, and applications.
763 *Multimedia Tools and Applications* 2011;51:303–339.
- 764 [33] Zhao R, Ouyang W, Li H, Wang X. Saliency Detection by Multi-Context Deep Learning. In: *Proceedings of the IEEE*
765 *Conference on Computer Vision and Pattern Recognition (CVPR)*; 2015. p. 1265–1274.
- 766 [34] Chu HJ, Wu CF, Lin YP. Incorporating spatial autocorrelation with neural networks in empirical land-use change models.
767 *Environment and Planning B: Planning and Design* 2013;40(3):384–404.
- 768 [35] Luo W, Li Y, Urtasun R, Zemel R. Understanding the effective receptive field in deep convolutional neural networks.
769 *Advances in neural information processing systems* 2016;29.
- 770 [36] Yang W, Tan RT, Feng J, Liu J, Guo Z, Yan S. Deep joint rain detection and removal from a single image. In: *Proceedings*
771 *of the IEEE conference on computer vision and pattern recognition*; 2017. p. 1357–1366.
- 772 [37] Liu YF, Jaw DW, Huang SC, Hwang JN. DesnowNet: Context-aware deep network for snow removal. *IEEE Transactions*
773 *on Image Processing* 2018;27(6):3064–3073.
- 774 [38] Heiskanen J, C B, N B, C C, H C, B G, et al. The Integrated Carbon Observation System in Europe. *Bulletin of the*
775 *American Meteorological Society* 2022;103(3):E855–E872.
- 776 [39] Juszczak T. Voluntary National report to UNF1 from Switzerland. United Nations, Department of Economic and Social
777 Affairs - Forests; 2019.
- 778 [40] Burri S. Long-Term Environmental Research–The Davos-Seehornwald Site. *ETH Zurich Research collection* 2019;.
- 779 [41] WSL. Long-term Forest Ecosystem Research (WSL); 2023.
- 780 [42] TreeNet. Biological drought and growth indicator network; 2023.
- 781 [43] ETH-Zurich. Biological drought and growth indicator network; 2023.
- 782 [44] ICOS. Integrated Carbon Observation System; 2023.

- 783 [45] ICP-Forest. International Co-operative Programme on Assessment and Monitoring of Air Pollution Effects on Forests;
784 2023.
- 785 [46] eLTER. Integrated European Long-Term Ecosystem, critical zone and socio-ecological Research; 2023.
- 786 [47] Revengea JC, Trepekli K, Oehmcke S, Jensen R, Li L, Igel C, et al. Above-Ground Biomass Prediction for Croplands at a
787 Sub-Meter Resolution Using UAV-LiDAR and Machine Learning Methods. *Remote Sensing* 2022;14(16):3912.
- 788 [48] Davidson L, Mills J, Haynes I, Augarde C, Bryan P, Douglas M. Airborne to UAS LiDAR: An analysis of UAS LiDAR
789 ground control targets. *ISPRS Geospatial Week* 2019;.
- 790 [49] Swiss Federal Institute for Forest S, (WSL) LR. Methods of the Sanasilva Inventory; 2023.
- 791 [50] Hunziker S, Begert M, Scherrer SC, Rigling A, Gessler A. Below average midsummer to early autumn precipitation
792 evolved into the main driver of sudden Scots pine vitality decline in the Swiss Rhône valley. *Frontiers in Forests and*
793 *Global Change* 2022;p. 103.
- 794 [51] ICOS-ETC. Instruction on ancillary vegetation measurements in forest; 2023.
- 795 [52] Chen Q GP Baldocchi D, M K. Isolating Individual Trees in a Savanna Woodland Using Small Footprint Lidar Data. In:
796 *Photogrammetric Engineering and Remote Sensing*, 72(8): 923-932; 2006. p. 923-932.
- 797 [53] GreenValley-International. LiDAR360 User Guide. California, USA; January 2021, www.greenvalletintl.com.
- 798 [54] Anselin L. Local indicators of spatial association—LISA. *Geographical analysis* 1995;27(2):93-115.
- 799 [55] Anselin L, Rey SJ. Perspectives on spatial data analysis. In: *Perspectives on spatial data analysis* Springer; 2010.p.
800 1-20.
- 801 [56] Breunig MM, Kriegel HP, Ng RT, Sander J. LOF: identifying density-based local outliers. In: *Proceedings of the 2000*
802 *ACM SIGMOD international conference on Management of data*; 2000. p. 93-104.
- 803 [57] Liu FT, Ting KM, Zhou ZH. Isolation forest. In: *2008 eighth iee international conference on data mining IEEE*; 2008.
804 p. 413-422.
- 805 [58] Anselin L, Syabri I, Kho Y. GeoDa: an introduction to spatial data analysis. In: *Handbook of applied spatial analysis:*
806 *Software tools, methods and applications* Springer; 2009.p. 73-89.
- 807 [59] Da Silva BC, Basso EW, Bazzan AL, Engel PM. Dealing with non-stationary environments using context detection. In:
808 *Proceedings of the 23rd international conference on Machine learning*; 2006. p. 217-224.
- 809 [60] Fu WJ, Jiang PK, Zhou GM, Zhao KL. Using Moran's I and GIS to study the spatial pattern of forest litter carbon density
810 in a subtropical region of southeastern China. *Biogeosciences* 2014;11(8):2401-2409.
- 811 [61] Cressie N. *Statistics for spatial data*. John Wiley & Sons; 2015.
- 812 [62] Getis A, Ord JK. The analysis of spatial association by use of distance statistics. In: *Perspectives on spatial data analysis*
813 Springer; 2010.p. 127-145.
- 814 [63] Westerholt R, Resch B, Mocnik FB, Hoffmeister D. A statistical test on the local effects of spatially structured variance.
815 *International Journal of Geographical Information Science* 2018;32(3):571-600.
- 816 [64] Hastie TJ. *Generalized additive models*. In: *Statistical models in S* Routledge; 2017.p. 249-307.
- 817 [65] Anselin L, et al. *Spatial econometrics. A companion to theoretical econometrics* 2001;310330.
- 818 [66] Beven KJ, Kirkby MJ. A physically based, variable contributing area model of basin hydrology/Un modèle à base
819 physique de zone d'appel variable de l'hydrologie du bassin versant. *Hydrological sciences journal* 1979;24(1):43-69.

- 820 [67] Mohamedou C, Tokola T, Eerikäinen K. LiDAR-based TWI and terrain attributes in improving parametric predictor for
821 tree growth in southeast Finland. *International journal of applied earth observation and geoinformation* 2017;62:183–
822 191.
- 823 [68] Kopecký M, Macek M, Wild J. Topographic Wetness Index calculation guidelines based on measured soil moisture and
824 plant species composition. *Science of the Total Environment* 2021;757:143785.
- 825 [69] ESRI. ArcGis Pro: Implementation Guide. Redlands, California; 2021, www.esri.com.
- 826 [70] Landini G. Particles8 class: An ImageJ plugin for estimating various statistics of binary 8- connected particles.; 2010.
- 827 [71] Güler C, Beyhan B, Tağa H. PolyMorph-2D: An open-source GIS plug-in for morphometric analysis of vector-based
828 2D polygon features. *Geomorphology* 2021;386:107755.
- 829 [72] Steiniger S, Blake L. OpenJUMP software; 2022.
- 830 [73] Freund Y, Schapire RE. A decision-theoretic generalization of on-line learning and an application to boosting. *Journal*
831 *of computer and system sciences* 1997;55(1):119–139.
- 832 [74] Friedman JH. Greedy function approximation: a gradient boosting machine. *Annals of statistics* 2001;p. 1189–1232.
- 833 [75] Schapire RE. Explaining adaboost. *Empirical Inference: Festschrift in Honor of Vladimir N Vapnik* 2013;p. 37–52.
- 834 [76] Tibshirani R. Regression shrinkage and selection via the lasso. *Journal of the Royal Statistical Society: Series B (Method-*
835 *ological)* 1996;58(1):267–288.
- 836 [77] Ho TK. Random decision forests. In: *Proceedings of 3rd international conference on document analysis and recognition,*
837 *vol. 1 IEEE; 1995. p. 278–282.*
- 838 [78] Vidaurre D, Bielza C, Larranaga P. A survey of L1 regression. *International Statistical Review* 2013;81(3):361–387.
- 839 [79] Demol M, Verbeeck H, Gielen B, Armston J, Burt A, Disney M, et al. Estimating forest above-ground biomass with
840 terrestrial laser scanning: Current status and future directions. *Methods in Ecology and Evolution* 2022;13(8):1628–
841 1639.
- 842 [80] Gryc V, Horáček P. Variability in density of spruce (*Picea abies* [L.] Karst.) wood with the presence of reaction wood.
843 *Journal of forest science* 2007;53(3):129–137.
- 844 [81] Scrinzi G, Galvagni D, Marzullo L. I nuovi modelli dendrometrici per la stima delle masse assestamentali in Provincia di
845 Trento. Provincia autonoma di Trento. Servizio foreste e fauna; 2010.
- 846 [82] Quionero-Candela J, Sugiyama M, Schwaighofer A, Lawrence ND. *Data Set Shift in Machine Learning*. MIT Press, Cam-
847 bridge, Massachusetts; 2009. [http://www.acad.bg/ebook/ml/The.MIT.Press.Dataset.Shift.in.Machine.Learning.](http://www.acad.bg/ebook/ml/The.MIT.Press.Dataset.Shift.in.Machine.Learning.Feb.2009.eBook-DDU.pdf)
848 [Feb.2009.eBook-DDU.pdf](http://www.acad.bg/ebook/ml/The.MIT.Press.Dataset.Shift.in.Machine.Learning.Feb.2009.eBook-DDU.pdf).
- 849 [83] Bates S, Hastie T, Tibshirani R. Cross-validation: what does it estimate and how well does it do it? *arXiv preprint*
850 *arXiv:210400673* 2021;.
- 851 [84] Altmann A, Toloşi L, Sander O, Lengauer T. Permutation importance: a corrected feature importance measure. *Bioin-*
852 *formatics* 2010;26(10):1340–1347.
- 853 [85] Wilcoxon F. *Individual comparisons by ranking methods*. Springer; 1992.
- 854 [86] Cliff N. Dominance statistics: Ordinal analyses to answer ordinal questions. *Psychological bulletin* 1993;114(3):494.
- 855 [87] Horton RE. Drainage-basin characteristics. *Transactions, American geophysical union* 1932;13(1):350–361.

- 856 [88] Zingg T. Beitrag zur schotteranalyse. PhD thesis, ETH Zurich; 1935.
- 857 [89] Buendia P, Soler C, Paolicchi F, Gago G, Urquieta B, Pérez-Sánchez F, et al. Morphometric characterization and
858 classification of alpaca sperm heads using the Sperm-Class Analyzer® computer-assisted system. *Theriogenology*
859 2002;57(4):1207–1218.
- 860 [90] Attneave F, Arnoult MD. The quantitative study of shape and pattern perception. *Psychological bulletin*
861 1956;53(6):452.
- 862 [91] Zăvoianu I. Morfometria bazinelor hidrografice. Editura Academiei Republicii Socialiste România; 1978.
- 863 [92] Miller VC. A QUANTITATIVE GEOMORPHIC STUDY OF DRAINAGE BASIN CHARACTERISTICS IN THE CLINCH
864 MOUNTAIN AREA VIRGINIA AND TENNESSEE. Columbia Univ New York; 1953.
- 865 [93] Schumm SA. Evolution of drainage systems and slopes in badlands at Perth Amboy, New Jersey. *Geological society of*
866 *America bulletin* 1956;67(5):597–646.
- 867 [94] Chorley RJ, Malm E Donald E, Pogorzelski HA. A new standard for estimating drainage basin shape. *American Journal*
868 *of Science* 1957;255:138–141.
- 869 [95] Horgan GW, Glasbey CA. Uses of digital image analysis in electrophoresis. *Electrophoresis* 1995;16(1):298–305.
- 870 [96] Zunic J, Rosin PL. A new convexity measure for polygons. *IEEE Transactions on Pattern Analysis and Machine Intelli-*
871 *gence* 2004;26(7):923–934.
- 872 [97] Rosin PL. Measuring rectangularity. *Machine Vision and Applications* 1999;11:191–196.
- 873 [98] Wadell H. Volume, shape, and roundness of quartz particles. *The Journal of Geology* 1935;43(3):250–280.
- 874 [99] Valladares F, Arrieta S, Aranda I, Lorenzo D, Sánchez-Gómez D, Tena D, et al. Shade tolerance, photoinhibition sensitivity
875 and phenotypic plasticity of *Ilex aquifolium* in continental Mediterranean sites. *Tree physiology* 2005;25(8):1041–
876 1052.
- 877 [100] Valladares F, Dobarro I, Sánchez-Gomez D, Pearcy RW. Photoinhibition and drought in Mediterranean woody saplings:
878 scaling effects and interactions in sun and shade phenotypes. *Journal of Experimental Botany* 2005;56(411):483–494.
- 879 [101] Pillar VD, Duarte LdS, Sosinski EE, Joner F. Discriminating trait-convergence and trait-divergence assembly patterns
880 in ecological community gradients. *Journal of Vegetation Science* 2009;20(2):334–348.
- 881 [102] Naesset E. Determination of mean tree height of forest stands using airborne laser scanner data. *ISPRS Journal of*
882 *Photogrammetry and Remote sensing* 1997;52(2):49–56.
- 883 [103] Guillén-Escribà C, Schneider FD, Schmid B, Tedder A, Morsdorf F, Furrer R, et al. Remotely sensed between-individual
884 functional trait variation in a temperate forest. *Ecology and Evolution* 2021;11(16):10834–10867.
- 885 [104] Zheng Z, Zeng Y, Schuman MC, Jiang H, Schmid B, Schaepman ME, et al. Individual tree-based vs pixel-based ap-
886 proaches to mapping forest functional traits and diversity by remote sensing. *International Journal of Applied Earth*
887 *Observation and Geoinformation* 2022;114:103074.
- 888 [105] Ma X, Migliavacca M, Wirth C, Bohn FJ, Huth A, Richter R, et al. Monitoring plant functional diversity using the
889 reflectance and echo from space. *Remote Sensing* 2020;12(8):1248.
- 890 [106] Wang CJ, Zhang ZX, Wan JZ. Vulnerability of global forest ecoregions to future climate change. *Global Ecology and*
891 *Conservation* 2019;20:e00760.
- 892 [107] He X, Zemel RS, Carreira-Perpinán MA. Multiscale conditional random fields for image labeling. In: *Proceedings of*
893 *the 2004 IEEE Computer Society Conference on Computer Vision and Pattern Recognition, 2004. CVPR 2004.*, vol. 2
894 IEEE; 2004. p. II-II.

- 895 [108] Yu F, Koltun V. Multi-scale context aggregation by dilated convolutions. arXiv preprint arXiv:151107122 2015;.
- 896 [109] Abelleira Martínez OJ, Fremier AK, Günter S, Ramos Bendaña Z, Vierling L, Galbraith SM, et al. Scaling up functional
897 traits for ecosystem services with remote sensing: concepts and methods. *Ecology and Evolution* 2016;6(13):4359–
898 4371.
- 899 [110] Goebes P, Schmidt K, Seitz S, Both S, Bruelheide H, Erfmeier A, et al. The strength of soil-plant interactions under
900 forest is related to a Critical Soil Depth. *Scientific Reports* 2019;9(1):8635.
- 901 [111] Green JK, Keenan TF. The limits of forest carbon sequestration. *Science* 2022;376(6594):692–693.
- 902 [112] Valladares F, Gianoli E, Gómez JM. Ecological limits to plant phenotypic plasticity. *New phytologist* 2007;176(4):749–
903 763.
- 904 [113] Kraft NJ, Adler PB, Godoy O, James EC, Fuller S, Levine JM. Community assembly, coexistence and the environmental
905 filtering metaphor. *Functional ecology* 2015;29(5):592–599.
- 906 [114] Strahler AN. Hypsometric (area-altitude) analysis of erosional topography. *Geological society of America bulletin*
907 1952;63(11):1117–1142.
- 908 [115] Berrar D. Cross-Validation. *Encyclopedia of Bioinformatics and Computational Biology* 2018;1:542–545.